Editors' Suggestion

Mitigation of exchange crosstalk in dense quantum dot arrays

Daniel Jirovec,[1,*,†] Pablo Cova Fariña,[1,*] Stefano Reale,[1] Stefan D. Oosterhout,[1,2] Xin Zhang,[1] Sander de Snoo,[1] Amir Sammak,[2] Giordano Scappucci,[1] Menno Veldhorst,[1] and Lieven M. K. Vandersypen[1,‡]

[1] *QuTech and Kavli Institute of Nanoscience, Delft University of Technology, 2600 GA Delft, Netherlands*
[2] *Netherlands Organisation for Applied Scientific Research (TNO), 2628 CK Delft, Netherlands*

(Received 28 March 2025; revised 4 June 2025; accepted 10 July 2025; published 19 September 2025)

Coupled spins in semiconductor quantum dots are a versatile platform for quantum computing and simulations of complex many-body phenomena. However, on the path of scale-up, crosstalk from densely packed electrodes poses a severe challenge. While crosstalk onto the quantum dot potentials is nowadays routinely compensated for, crosstalk on the exchange interaction is much more difficult to tackle because it is not always directly measurable. Here we propose and implement a way of characterizing and compensating crosstalk on adjacent exchange interactions by following the singlet-triplet avoided crossing in Ge. We show that we can easily identify the barrier-to-barrier crosstalk element without knowledge of the particular exchange value in a 2×4 quantum dot array. We uncover striking differences among these crosstalk elements that can be linked to the geometry of the device and the barrier gate fan-out. We validate the method by tuning up four-spin Heisenberg chains. The same method should be applicable to longer chains of spins and to other semiconductor platforms in which mixing of the singlet and the lowest-energy triplet is present or can be engineered. Additionally, this procedure is well-suited for automated tuning routines as we obtain a standout feature that can be easily tracked and directly returns the magnitude of the crosstalk.

DOI: 10.1103/qgnt-n527

I. INTRODUCTION

Spin qubits in gate-defined semiconductor quantum dots constitute a versatile platform for quantum computation owing to their long coherence times, demonstrated high-fidelity single-qubit and two-qubit gates, and their small footprint [1,2]. Also, they find applications in quantum simulations due to the inherent tunability of most Hamiltonian parameters, which allows the exploration of different limits of the Fermi-Hubbard model and the Heisenberg model [3]. A challenge in scaling up, however, is crosstalk from the gates defining the potential landscape as sketched in Fig. 1(a). Several approaches for crosstalk management exist and rely on defining a set of virtual gates designed to control the energy scale of choice, be it the on-site potential, the tunnel coupling, or the exchange interaction [4–8]. Virtual plunger gates controlling the on-site potential are nowadays routinely used in experiments [Fig. 1(b)], but methods for barrier-to-barrier crosstalk compensation are typically overlooked [Fig. 1(c)] and only rarely implemented [9,10].

Digital spin qubit experiments so far circumvent the problem by avoiding the simultaneous activation of adjacent exchange couplings [11,12] or by populating quantum dot arrays only sparsely [13–15]. When only one exchange interaction is activated at a time, any crosstalk to other exchanges will not induce a detrimental effect, because the exponential dependence of exchange strength on barrier voltage leads to a wide voltage range over which the other interactions are effectively switched "off." However, implementations of three-qubit gates have been shown and do require simultaneously activated adjacent exchange couplings [16,17]. Moreover, quantum simulation of the rich variety of physical phenomena described by the Fermi-Hubbard model [18–27] requires dense arrays of quantum dots with precise and ideally orthogonal control not only of the on-site potentials but also of the nearest-neighbor exchange interactions or tunnel couplings.

To appreciate why this is not straightforward, we note that once three or more spins are coupled together, the resulting energy spectrum and, hence, the oscillation

*These authors contributed equally to this work.
†Contact author: d.jirovec@tudelft.nl
‡Contact author: l.m.k.vandersypen@tudelft.nl

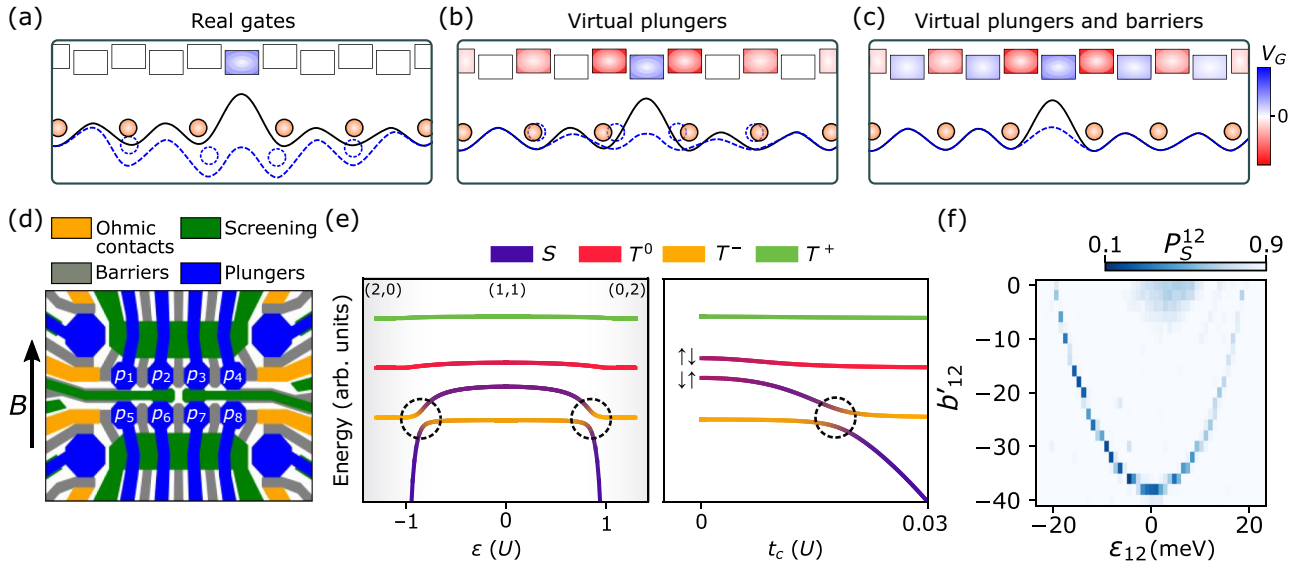

FIG. 1. (a) Confinement potential for a chain of charges defined by the top gates in real voltage space (solid black line). A negative voltage pulse on the central barrier gate not only causes the middle tunnel barrier to be lowered but also shifts the electrochemical potentials of the nearby quantum dots and the height of adjacent tunnel barriers (dashed blue line). (b) Commonly used virtual plunger gates work by application of a linear combination of gate voltages that keeps the electrochemical potentials of all other quantum dots fixed. However, adjacent tunnel barrier heights are still affected and lateral shifts of charges are still present, although they might be slightly reduced. (c) If also the barriers are virtualized, a pulse on the middle barrier gate is compensated by suitable pulses on other barrier gates to keep the other tunnel barriers fixed and, ideally, counteract the lateral shifts of charges. In practice, however, only the combined effect of lateral shifts and tunnel barrier alterations can be compensated. A correct virtualization should allow orthogonal control of exchange interactions and enable a straightforward tuning of multispin chains. (d) The 2×4 quantum dot array we use in this experiment. The quantum dot plungers are labeled as p_i. Barriers b_{ij} separate quantum dots i and j. The external magnetic field B is applied in an in-plane direction marked by the arrow. (e) Energy level diagram of a two-spin system in a double quantum dot as a function of detuning ϵ (left) and tunnel coupling t_c (right). The dashed circles mark the spin-orbit-induced avoided crossings. U is the charging energy. At $|\epsilon| > U$ the two charges occupy the same quantum dot [(2,0) and (0,2) charge regions]. For $|\epsilon| < U$ the charges are shared between the two adjacent quantum dots, and the energy splittings are determined by the respective Zeeman energies and the exchange interaction. The position of the avoided crossing is influenced by ϵ and t_c. (f) Measurement of the avoided crossing as a function of detuning and barrier voltage of Q_{12}, as described in the main text. The avoided crossing always occurs when $J = E_{T^-}$, constituting a constant-exchange feature that we are able to follow as a sharp reduction in singlet return probability P_S^{12}. At more positive values of b'_{12}, S-T^0 oscillations cause a reduced singlet return probability as well. As the barrier becomes more negative, the exchange increases, pushing the avoided crossing feature to smaller ϵ_{12}. At $\epsilon_{12} = 0$ all the exchange is induced by the barrier voltage b'_{12}.

frequencies are typically a combination of all the exchanges involved, hindering independent calibration of the exchange couplings. Furthermore, whereas the local electrochemical potentials vary linearly with the gate voltages, the tunnel coupling and exchange interaction depend exponentially on the gate voltage. To realize crosstalk compensation in the face of this exponential dependence, it was assumed in Refs. [6,28] that barrier-to-barrier crosstalk can be compensated by a linear combination of voltages in the *argument* of the exponential function, reducing crosstalk compensation between barriers to a linear problem nonetheless. In both cases, the virtualization methods required repeated measurements of either the tunnel coupling or exchange oscillations. Crosstalk was then extracted from exponential fits, resulting in an indirect, laborious, and potentially error-prone measure. It is therefore desirable to obtain a measure of the crosstalk in a direct way similar to reservoir addition lines used to virtualize plunger gates.

Here we demonstrate a way of characterizing barrier-to-barrier crosstalk to allow individual control of exchange interactions in a dense array of quantum dots. The method consists of tracking the position of the singlet-triplet anticrossing in the multidimensional voltage space spanned by the confining barrier gates. Such a feature can be induced by a suitable intrinsic spin-orbit interaction, local magnetic field gradients, or differences in the g tensors, and determines a point of constant exchange that is fast to measure and easy to identify. This is especially useful because it isolates the effect of the exchange interaction of interest and could also be adapted for automated optimizations [7]. We empirically find how the gate architecture affects

the crosstalk in the device. Finally, we apply this method to the tuning of four-spin Heisenberg chains in different configurations to test its validity and limitations.

II. DEVICE AND ENERGY DIAGRAM

The device consists of a 2×4 array of gate-defined quantum dots in a Ge/Si-Ge heterostructure [29] [Fig. 1(d); further details can be found in Appendix A]. Four sensors at the corners of the device enable fast charge sensing via radio-frequency tank circuits (the inductors are off-chip Nb-Ti-N coils, while the capacitance stems from parasitic capacitances) bonded directly to one of the Ohmic contacts of the respective sensor [30]. The potential landscape is tuned by means of dc voltages to form eight quantum dots, each containing a single hole, under the plunger gates p_i, with $i \in [1, 8]$, except for quantum dot 2, where, for practical reasons, we confine three holes. The inter-quantum-dot barrier gates b_{ij} separate quantum dots i and j. Quantum dots 1, 4, 5 and 8 have additional barriers to the reservoirs. Except for b_{26} and b_{37}, all the barriers are deposited in the first gate layer, allowing strong exchange tunability, unlike in previous experiments on 2×4 Ge/Si-Ge quantum dot arrays [31,32] (see Appendix G). Importantly, since the charge carriers are holes, accumulation voltages are negative. A typical dc voltage configuration of the tuned-up device is reported in Fig. 7 in Appendix A. All the plunger gates and inter-quantum-dot barrier gates are connected also to an arbitrary waveform generator (AWG), via bias tees and attenuated coaxial transmission lines, to allow fast pulsing away from the dc voltage configuration. In all measurements, the reported voltage amplitudes are the attenuated AWG amplitudes at the gates, without the dc component.

Throughout the experiments we work with virtualized plunger gates (p_i') that are designed to vary the electrochemical potential of quantum dot i while keeping the electrochemical potential of all other quantum dots fixed [4,7]. The barrier gates are at first virtualized against the electrochemical potentials only, and we denote them as b_{ij}'. This ensures that a pulse on a virtual barrier keeps the quantum dot potentials unchanged [see Figs. 1(a) and 1(b)]. We further define a detuning axis $\epsilon_{ij} = ap_i' - bp_j'$ and an electrochemical potential axis $\mu_{ij} = cp_i' + dp_j'$, with a, b, c, and d experimentally determined coefficients (see Appendix B for details on the transformations between real and virtual gate voltages). Every double quantum dot is capable of hosting a singlet-triplet (S-T) qubit [33–35], which we label Q_{ij}, with i and j (we choose $i < j$) denoting the first quantum dot and the second quantum dot in the pair, respectively. To operate S-T qubits, precise control of the exchange interaction J_{ij} is required (in the following discussion we omit the indices ij and reintroduce them when necessary). In quantum dot systems, J originates from the wave-function overlap of and the Coulomb repulsion between neighboring spins [6,36] and can be controlled by means of ϵ and tunnel coupling t_c, taking the form

$$J(\epsilon, b') = \frac{4t_c^2(b')U}{(U^2 - \epsilon^2)}$$

for $J \ll U$, where U is the charging energy [37]. The tunnel coupling is itself a function of the barrier voltage, and because of crosstalk, also of the voltage on neighboring barriers. We seek to compensate for this crosstalk in Sec. IV to obtain orthogonal control of exchange interactions. We point out we do not attempt to compensate for the effect of plunger voltages on the exchange, as the inter-quantum-dot detuning is an explicit and desired control knob for the exchange strength, especially during readout and initialization.

A typical energy diagram as a function of ϵ with finite t_c of an S-T qubit is depicted in the left panel of Fig. 1(e). Unless indicated otherwise, we operate every qubit at its symmetry point $\epsilon = 0$, where the exchange reduces to $J(b') = 4t_c^2(b')/U$ and is, therefore, controlled only by the barrier voltage [38]. The energy diagram in this case is depicted in the right panel of Fig. 1(e).

In contrast to previous work [31], here we do not measure t_c and U; rather, we assume an empirical dependence of J on the designated barrier:

$$J(b') = J_0 \exp(k(b' - b_0')),$$

where $J_0 = 1$ MHz, k represents the exponential lever arm of the barrier, and b_0' is an offset that depends on the particular dc voltage configuration. The dc configuration of the barriers is tuned in a way that ensures b_0' is relatively small such that the voltage pulses from the AWG are capable of inducing a considerable on:off ratio for each exchange (in general, we find $|b_0'| < 40$ mV; see Appendix G). Assuming zero residual exchange at the symmetry point, the four eigenstates are the polarized triplets $|T^-\rangle = |\downarrow\downarrow\rangle$ and $|T_+\rangle = |\uparrow\uparrow\rangle$, with energies $E_{T^\pm} = \pm\sum E_Z = \pm\sum g\mu_B B$, and the antiparallel states $|\uparrow\downarrow\rangle$ and $|\downarrow\uparrow\rangle$, with energies $E_{\mathrm{AP}} = \pm\frac{\Delta E_Z}{2} = \pm\frac{\Delta g \mu_B B}{2}$, where g is the effective g factor of each of the quantum dots that we measure and takes values between 0.3 and 0.45 in the in-plane magnetic field direction (see Fig. 19), consistent with previously reported values for holes in Ge [16], μ_B is the Bohr magneton, and $B = 10$ mT is the external magnetic field applied approximately in the in-plane direction. At large exchange J, the antiparallel states are no longer eigenstates of the Hamiltonian, being replaced by $|S\rangle = \frac{|\uparrow\downarrow\rangle - |\downarrow\uparrow\rangle}{\sqrt{2}}$ and $|T^0\rangle = \frac{|\uparrow\downarrow\rangle + |\downarrow\uparrow\rangle}{\sqrt{2}}$. Finally, the spin-orbit spin-flip term Δ_{SO} couples $|S\rangle$ and $|T^-\rangle$, as highlighted by the dashed circles in Fig. 1(e) [39,40]. At these avoided crossings, coherent S-T^- oscillations can be induced [32,41].

In the (2,0) charge configuration, the energy splitting between $|S(2,0)\rangle$ and $|T(2,0)\rangle$ well exceeds the thermal energy, enabling fast initialization in the singlet ground state. The different energy scales of the system then allow us to initialize target eigenstates by appropriately choosing the ramp time from the (2,0) charge configuration to the (1,1) charge symmetry point (see Appendix E). For readout, we rely on Pauli spin blockade (PSB). The rather small external magnetic field ensures that only the singlet state is unblocked in the PSB region, as opposed to parity readout, where both antiparallel spin states are typically unblocked [42]. This enables the discrimination of $|S\rangle$ from the triplets by our monitoring the charge sensor in single-shot readout.

In Fig. 1(f) we experimentally map out the S-T^- avoided crossing as a function of ϵ_{12} and b'_{12} by initializing $|S\rangle$ in Q_{12} and recording the probability of retrieving $|S\rangle$. In between, we rapidly pulse detuning to (1,1), let the system evolve for 50 ns, corresponding approximately to flipping the initial $|S\rangle$ to $|T^-\rangle$ at the avoided crossing, and pulse detuning back to (2,0) for readout. We can identify the position of the S-T^- avoided crossing by a sharp reduction in P_S. Since at this position $J(\epsilon, b') = E_{T^-}$, the avoided crossing constitutes a constant-exchange feature. The symmetric U shape is confirmation that the virtualization of b'_{12} against the plunger gates is accurate as we would otherwise find a skewed shape [32] (see Fig. 10 in Appendix B). For more-positive barrier voltages we also observe a reduction of P_S, which can be attributed to S-T^0 oscillations at low J. Importantly, the lack of additional features around the avoided crossing allows us to unambiguously and precisely identify its location.

III. EXCHANGE CROSSTALK

Before discussing how to correct for crosstalk, we elucidate how exchange interactions are affected by nearby barrier voltages. As an example, consider the left side of the device. Figure 2(a) shows exchange oscillations in Q_{56} as a function of b'_{15}, with b'_{56} kept at a constant, negative value [see Fig. 2(c)]. We initialize Q_{56} in $|\downarrow\uparrow\rangle$ and Q_{12} in $|\downarrow\downarrow\rangle$ and record the final state probability $P^{56}_{\downarrow\uparrow}$ as a function of dwell time τ. At first, b'_{56} is the only gate inducing exchange between the spins in quantum dots 5 and 6, leading to the oscillation seen in the top part of Fig. 2(a). As we pulse b'_{15} more negative, we first see the frequency of the oscillations reduce, a clear example of crosstalk. Furthermore, we also see another frequency appearing below $b'_{15} = -20$ mV [see also the FFT in Fig. 2(b)]. This is an indication that b'_{15} now induces exchange between quantum dots 5 and 1. In such a situation it is not clear which of the measured frequency shifts can be attributed to the activation of J_{15} or to crosstalk on J_{56}. Without further modeling, it is, therefore, not possible to quantify the effect of b'_{15} on J_{56} in this voltage range. We can only reliably extract the crosstalk for $b'_{15} > -20$ mV (e.g., before we induce any measurable exchange J_{15}).

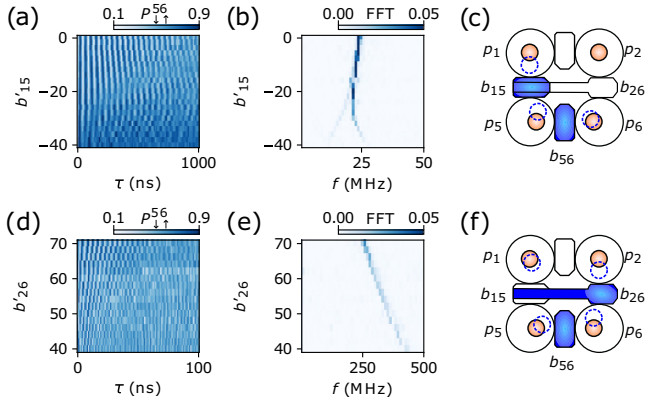

FIG. 2. (a) Exchange oscillations in Q_{56} as a function of b'_{15} and dwell time τ, as explained in the main text. (b) FFT of (a). We clearly see that the main frequency is reduced and for more negative values of b'_{15} a second oscillation frequency appears. The frequency reduction is a sign of crosstalk, and the appearance of a second frequency is due to a finite J_{15}. (c) Sketch of the experiment corresponding to (a). The orange circles depict the approximate charge positions when only b'_{56} induces exchange. The dashed blue circles represent the shifted quantum dot positions as we open b'_{15}. (d) Exchange oscillations in Q_{56} as a function of b'_{26} and dwell time τ. (e) FFT of (d). We see a change in frequency of about 60% over only 30 mV, indicating strong crosstalk. (f) Sketch of the experiment corresponding to (d). The fan-out of b_{26} leads to much larger crosstalk than for b_{15} and may affect the position of all nearby charges.

A similar experiment is reported in Figs. 2(d)–2(f). However, in this case we apply a pulse on b'_{26} (b'_{56} is more negative than in Fig. 2(a), leading to much faster oscillations). While here we do not see another frequency appear because we do not apply a large enough pulse on b'_{26}, we observe a change in frequency of about 60% in a range of only 30 mV, indicating very strong crosstalk. This might be due to the fan-out of b_{26}, as highlighted in the sketch in Fig. 2(f). While this measurement reveals the crosstalk from b'_{26} onto J_{56}, it does not tell us how to compensate for it. In the next section we show how exchange crosstalk can be extracted directly and compensated.

IV. CHARACTERIZATION OF EXCHANGE VIRTUALIZATION PARAMETERS

We now show how we can leverage the S-T^- avoided crossing to directly extract the crosstalk matrix element for barrier-to-barrier crosstalk compensation. At the avoided crossing, with $\epsilon_{ij} = 0$, all the exchange is induced by the virtual barrier gate voltage b'_{ij} satisfying $|J(b'_{ij})| = |E_{T^-_{ij}}|$ and is to first order insensitive to small variations of ϵ_{ij}. Moreover, any unintentional variation in ϵ_{ij} will only

increase J_{ij}, but never decrease it as in the case of lateral shifts of the quantum dot positions. To compensate exchange crosstalk we introduce a second layer of virtualization and define new virtual barrier voltages as $b^{\dagger}_{ij}$. As in previous work [6,28] we assume a linear barrier crosstalk and an exponential dependence of J on the new virtual barrier: $J_{ij} = J_0 \exp(k(b^{\dagger}_{ij} - b^{\dagger}_{0,ij}))$ and $b^{\dagger}_{ij} = \sum_{mn} \alpha^{mn}_{ij} b'_{mn}$, where nm are all the tuples corresponding to adjacent spins and $\alpha^{mn}_{ij} = \frac{\delta J_{ij}}{\delta b'_{mn}} / \frac{\delta J_{ij}}{\delta b'_{ij}}$. The term $b^{\dagger}_{0,ij}$ is an offset in $b^{\dagger}_{ij}$ that we need to quantify only when calibrating the dependence of J on $b^{\dagger}_{ij}$. For crosstalk compensation, we therefore need to determine all the values α^{mn}_{ij}, where by definition $\alpha^{ij}_{ij} = 1$. Since the avoided crossing constitutes a constant-exchange feature, we can track its position as a function of b'_{mn} and b'_{ij} and extract a slope returning $-\alpha^{mn}_{ij}$ directly, without the need to extract $\frac{\delta J_{ij}}{\delta b'_{mn}}$ with exponential fits through a series of data points. This is the main advantage of the method presented here.

Figure 3(a) shows measurements of the avoided crossing of Q_{56} as a function of b'_{56} and all other b'_{mn}. The position of the avoided crossing is reflected by a sharp reduction in P_S. In all plots we can follow this standout feature with Gaussian fits and extract the dashed red lines (see Appendix C). The linear slopes confirm the assumption that barrier gate crosstalk is linear, at least in this regime. The value of the slope $\frac{\delta b'_{56}}{\delta b'_{mn}}$ directly returns the crosstalk element α^{mn}_{56}.

By plugging α^{mn}_{56} into the correction matrix and repeating the measurements in Fig. 3(a) as a function of $b^{\dagger}_{56}$ and $b^{\dagger}_{mn}$ [Fig. 3(b)], we now observe completely vertical constant-exchange features, controlled exclusively by $b^{\dagger}_{56}$, as intended. The bottom-left panel in Fig. 3(b) further confirms that the crosstalk is compensated as we record exchange oscillations of Q_{56} as a function of all the $b^{\dagger}_{mn}$ except $b^{\dagger}_{56}$ and observe no change in frequency for the voltage ranges considered here. Note that the voltage range of $b^{\dagger}_{12}$ we scan here corresponds to an on:off ratio of J_{12} of more than 100. Similar ratios apply to J_{23}, J_{34}, J_{48}, and J_{78} and their respective virtual barrier gates. This shows that for nonadjacent exchange interactions, the gate crosstalk can be efficiently compensated over at least 2 orders of magnitude. The virtual barriers $b^{\dagger}_{15}$, $b^{\dagger}_{26}$, and $b^{\dagger}_{67}$ are scanned over a range chosen as to not induce any exchange, since this would alter the position of the avoided crossing even without crosstalk (see Fig. 2). We show in Sec. V how to test whether the virtualization remains effective also when adjacent exchanges are turned on.

We find correction factors for every gate where we were able to induce exchange, always taking care that

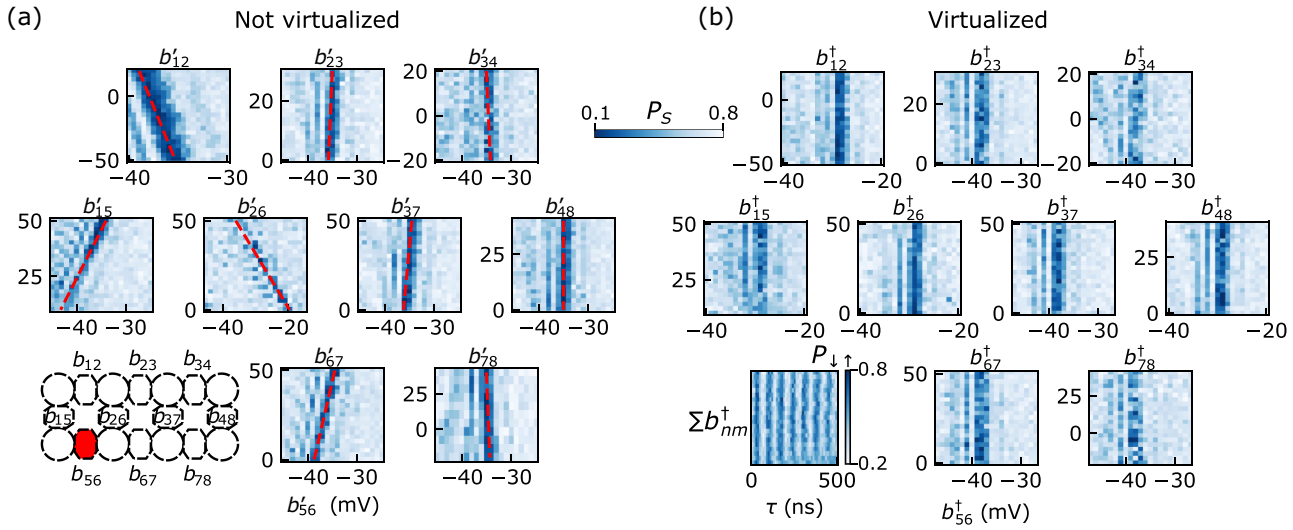

FIG. 3. (a) S-T^{-} avoided crossing of Q_{56} as a function of b'_{56} on the horizontal axis and all the other barriers on the respective vertical axis. The plots are ordered to reflect the geometric location of the stepped gate. The position of the avoided crossing is reflected by a sharp decrease of the singlet return probability (see the main text). From the fitted red dashed lines we extract the crosstalk elements α^{mn}_{56}. The fact that we can fit all crosstalk features with a linear function confirms the assumption of linear barrier crosstalk. (b) S-T^{-} avoided crossing of Q_{56} as a function of $b^{\dagger}_{56}$ on the horizontal axis and all the other virtual barriers on their respective vertical axis. After the virtualization process the S-T^{-} avoided crossing position is controlled only by $b^{\dagger}_{56}$ as intended. To further verify that the exchange remains stable, we plot exchange oscillations of Q_{56} at the bottom left. We vary all the virtual barriers except $b^{\dagger}_{56}$ together in the same range as in the individual plots. As desired, the exchange oscillations do not change in the ranges considered here. We repeat the same procedure on the other barrier gates (see Appendix D) and successively fill in the values for α^{mn}_{ij}.

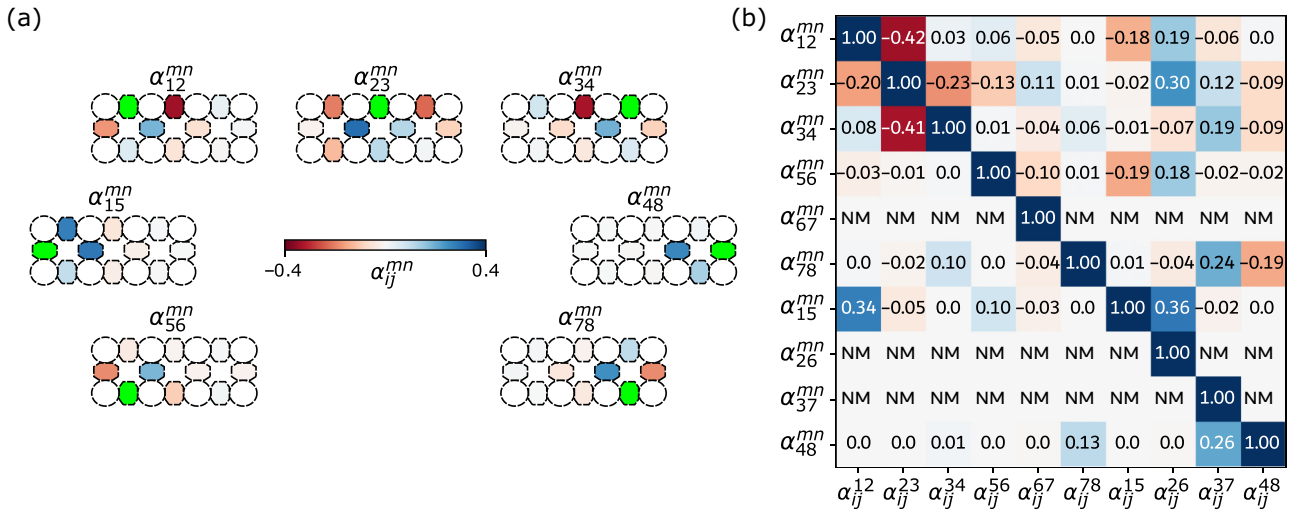

FIG. 4. (a) Exchange crosstalk elements α_{ij}^{mn} extracted for the barriers highlighted in bright green. We clearly see a reduction of crosstalk with distance as we expect for capacitive crosstalk. Positive (negative) crosstalk elements imply that an adjacent barrier gate enhances (reduces) a given exchange coupling. (b) Virtual gate matrix for the barrier gates showing α_{ij}^{mn}, summarizing the results from (a). Except for α_{26}^{mn}, α_{37}^{mn}, and α_{67}^{mn}, all the elements α_{ij}^{mn} are measured. In the experiment the elements labeled "NM" (for "not measured") are replaced by 0. To be clear, this matrix reports how much each b_{ij}' affects the various $b_{mn}^{\dagger}$. The barrier gate voltages b_{ij}' needed to orthogonally control the respective exchange interactions via $b_{mn}^{\dagger}$ are obtained from the inverse of this matrix.

nearest-neighbor gates do not induce any exchange. For practical reasons we did not characterize virtualization of $b_{26}^{\dagger}$, $b_{37}^{\dagger}$, and $b_{67}^{\dagger}$ but characterized only their effect on other gates. The fan-out of b_{26} and b_{37} affects the charge sensors and results in a loss of the readout signal, while a too negative voltage in b_{67} accumulates spurious quantum dots that couple to the spins in quantum dots 5 and 6. These problems will be addressed in future device generations.

Figure 4(a) color-codes the extracted crosstalk elements and shows their geometric distribution with respect to the gate that is being virtualized (highlighted by the bright green color). We clearly observe a decay of $|\alpha_{ij}^{mn}|$ with distance as expected. We note that crosstalk between barriers that are side by side along the legs of the ladder is negative, similarly to what was found in previous work [5,6]. In contrast, crosstalk between barriers oriented orthogonal to each other can also be positive, which is an indication that lateral shifts of the quantum dot positions are less important. Finally, many α_{ij}^{26} and α_{ij}^{37} are relatively large, sometimes exceeding 30% [see Fig. 4(b)], which suggests that the fan-out of their respective gates, b_{26} and b_{37}, can induce considerable crosstalk [see Fig. 1(d) and Fig. 6 in Appendix A]. This fact should be taken into account when future devices are being designed.

In the crosstalk extraction we have not considered g-factor modulation due to detuning and barrier gate voltages [43]. Moreover, we note that occasionally we have to slightly correct the initially extracted virtualization matrix element [Fig. 4(b)] to obtain an accurate crosstalk compensation.

Finally, we note that this method is suitable when exchange values are of the same order as the Zeeman energy. For $|J| \ll |E_{T^-}|$, which is the case for high external magnetic field operation, there is no avoided crossing to follow. To circumvent this, one could determine the crosstalk elements at low external field and then perform the desired experiments at higher field. Alternatively, it might be possible to use microwave driving to track the dependence of the spin resonance frequency. Indeed, the resonance frequency of a spin is modified by the exchange interaction, so it would be possible to fix the applied microwave tone and scan the desired barrier against all other barriers and extract α_{ij}^{mn} in the same way we did here.

In the following we explore whether α_{ij}^{mn} is stable even when nearest-neighbor exchanges are turned on. This is a crucial question as it would allow extending spin chains indefinitely after locally mitigating crosstalk.

V. VALIDATION OF THE VIRTUALIZATION IN EXTENDED SPIN CHAINS

To test if the virtualization parameters are still valid in a regime where nearest-neighbor exchanges are turned on, we proceed to couple four spins into a chain and observe the resulting oscillation dynamics. As shown in Figs. 2(a) and 2(b), activated nearest-neighbor interactions result in a highly nontrivial time evolution with multiple visible oscillation frequencies. However, preparing special states and evolving them at special voltage points results in a single visible oscillation frequency that we use here to validate the virtualization. For a chain of coupled spins, the

Hamiltonian describing the system can be approximated as [44]

$$H = \sum_i g_i \mu_B B S_{z,i} + \sum_i \Delta_{SO,i} S_{x,i} + \sum_{\langle i,j \rangle} J_{ij} \left(\mathbf{S}_i \mathbf{S}_j - \frac{1}{4} \right), \tag{1}$$

where $\mathbf{S} = (S_x, S_y, S_z) = \hbar/2(\sigma_x, \sigma_y, \sigma_z)$ is the vector of spin operators with the Pauli matrices σ_x, σ_y, and σ_z for each spin and the indices i and j run over nearest neighbors, and we set $\hbar = 1$. The additional term Δ_{SO} stems from intrinsic spin-orbit interaction and the anisotropic g tensors [32]. Ignoring the spin-orbit term and considering four adjacent spins, we can conveniently write Eq. (1) in the reduced basis $\left\{ |S_{ij} S_{kl}\rangle, |S_{ij} T^-_{kl}\rangle, |T^-_{ij} S_{kl}\rangle, |T^-_{ij} T^-_{kl}\rangle \right\}$ as

$$H = H_Q = \begin{pmatrix} -J_{ij} - J_{kl} & 0 & 0 & 0 \\ 0 & -J_{ij} - \overline{E}_{z,kl} & -\frac{J_{jk}}{2} & 0 \\ 0 & -\frac{J_{jk}}{2} & -\overline{E}_{z,ij} - J_{kl} & 0 \\ 0 & 0 & 0 & -\overline{E}_{z,ijkl} + \frac{J_{jk}}{2} \end{pmatrix}. \tag{2}$$

We want to draw attention to the matrix elements that involve $|S_{ij} T^-_{kl}\rangle$ and $|T^-_{ij} S_{kl}\rangle$. When $|J_{ij} - \overline{E}_{z,ij}| = |J_{kl} - \overline{E}_{z,kl}|$, the diagonal elements are equal and the resulting degeneracy is lifted by the off-diagonal elements $-J_{jk}/2$. We call this the resonant ST^- condition. Initializing one of the two states $|S_{ij} T^-_{kl}\rangle$ or $|T^-_{ij} S_{kl}\rangle$, and letting the system evolve at this special point, results in $|ST^-\rangle \leftrightarrow |T^- S\rangle$ oscillations with frequency $hf = J_{jk}$. This convenient feature was exploited in Ref. [32] to implement a two-qubit gate for singlet-triplet qubits and in Ref. [26] to estimate the exchange interaction in a four-qubit plaquette. Similar arguments hold for the $\left\{ |S_{ij} S_{kl}\rangle, |S_{ij} T^0_{kl}\rangle, |T^0_{ij} S_{kl}\rangle, |T^0_{ij} T^0_{kl}\rangle \right\}$ subspace, where the resonant condition appears when $\sqrt{J_{ij}^2 + \Delta E_{z,ij}^2} = \sqrt{J_{kl}^2 + \Delta E_{z,kl}^2}$. We use these resonant conditions to verify whether the virtualization obtained with nearest-neighbor couplings switched off is still valid when nearest-neighbor interactions are turned on. This test relies on the fact that the position of the resonant condition depends on both $J_{ij}(b^\dagger_{ij})$ and $J_{kl}(b^\dagger_{kl})$ (as well as the Zeeman energies), while the oscillation frequency depends on $J_{jk}(b^\dagger_{jk})$. Hence, we can test whether we find the resonant condition at the correct location and whether the oscillation frequency matches our expectations (more details can be found in Appendix H).

We study three implementations of a four-spin chain with nearest-neighbor couplings: chain 3-4-8-7, chain 2-1-5-6, and chain 1-2-3-4. In the first two cases, the chains are curved around the right and left edges of the device, respectively, while in the last case the quantum dots forming the chain are assembled linearly. The latter situation was previously studied in GaAs devices in Refs. [6,28].

We first consider the chain 3-4-8-7. After having extracted the crosstalk coefficients α^{mn}_{34}, α^{mn}_{48}, and α^{mn}_{78}, we measure exchange oscillations for Q_{34}, Q_{48}, and Q_{78} as a function of $b^\dagger_{34}$, $b^\dagger_{48}$, and $b^\dagger_{78}$, respectively, to extract the dependence $J_{ij}(b^\dagger_{ij})$. For these measurements, the other exchange interactions are turned off such that the oscillation frequency depends only on the exchange interaction of interest. We then fit the oscillation frequency to

$$f_{ij}(b^\dagger_{ij}) = \sqrt{\left(J_0 \exp\left\{ k_{ij} (b^\dagger_{ij} - b^\dagger_{0,ij}) \right\} \right)^2 + \Delta E^2_{Z,ij}} \tag{3}$$

with k_{ij}, $b^\dagger_{0,ij}$, and $\Delta E_{Z,ij}$ as free parameters (see Fig. 20 in Appendix G). With the knowledge of these exchange dependencies as well as the Zeeman energies, we are able to predict at which voltage points $(b^\dagger_{34}, b^\dagger_{78})$ the resonant conditions should appear. Figure 5(a) shows the resonant ST^- condition as a function of $b^\dagger_{34}$ and $b^\dagger_{78}$ with the exchange in between set to $J_{48} \approx 2$ MHz through $b^\dagger_{48}$. We initialize $|S_{78} T^-_{34}\rangle$ and let the system evolve for $\tau = 380$ ns at each voltage point, which ensures an approximate population inversion to $|T^-_{78} S_{34}\rangle$ at the resonant condition as long as J_{48} remains unaffected by $b^\dagger_{34}$ and $b^\dagger_{78}$. We identify the resonant condition as a sharp change in return probability. We do not record the joint probability of measuring $|S_{34} T^-_{78}\rangle$, but rather choose to measure only P^{34}_S. By operating in regimes where leakage outside the $|ST^-\rangle, |T^- S\rangle$ subspace is suppressed, we still recover the desired information. The dotted red line is the predicted location of the resonant condition based on the extracted exchange dependencies and the Zeeman energies, which agrees well with the data. Numerical simulations of P^{34}_S resulting from the full system dynamics also match the experimental data very well [see Fig. 23(a) in Appendix I 1]. This suggests that $J_{34}(b^\dagger_{34})$ and $J_{78}(b^\dagger_{78})$ are still well virtualized even when J_{48} is activated.

To extract the value of J_{48} at a given voltage point, we can record the dynamics at the resonant condition. To do this, we choose any point along the resonant condition, away from any leakage features, and sweep $b^\dagger_{34}$ ($b^\dagger_{78}$) by ± 5 mV (∓ 5 mV), here resulting in the dashed black line in Fig. 5(a), as a function of the dwell time. In Fig. 5(b) we clearly see a chevron pattern with a maximum in amplitude, corresponding to the resonant condition, oscillating at a frequency given by J_{48}. This frequency agrees well with the corresponding frequency seen in numerical simulations [see Fig. 23(b) in Appendix I 1], providing evidence that also $b^\dagger_{48}$ is properly virtualized.

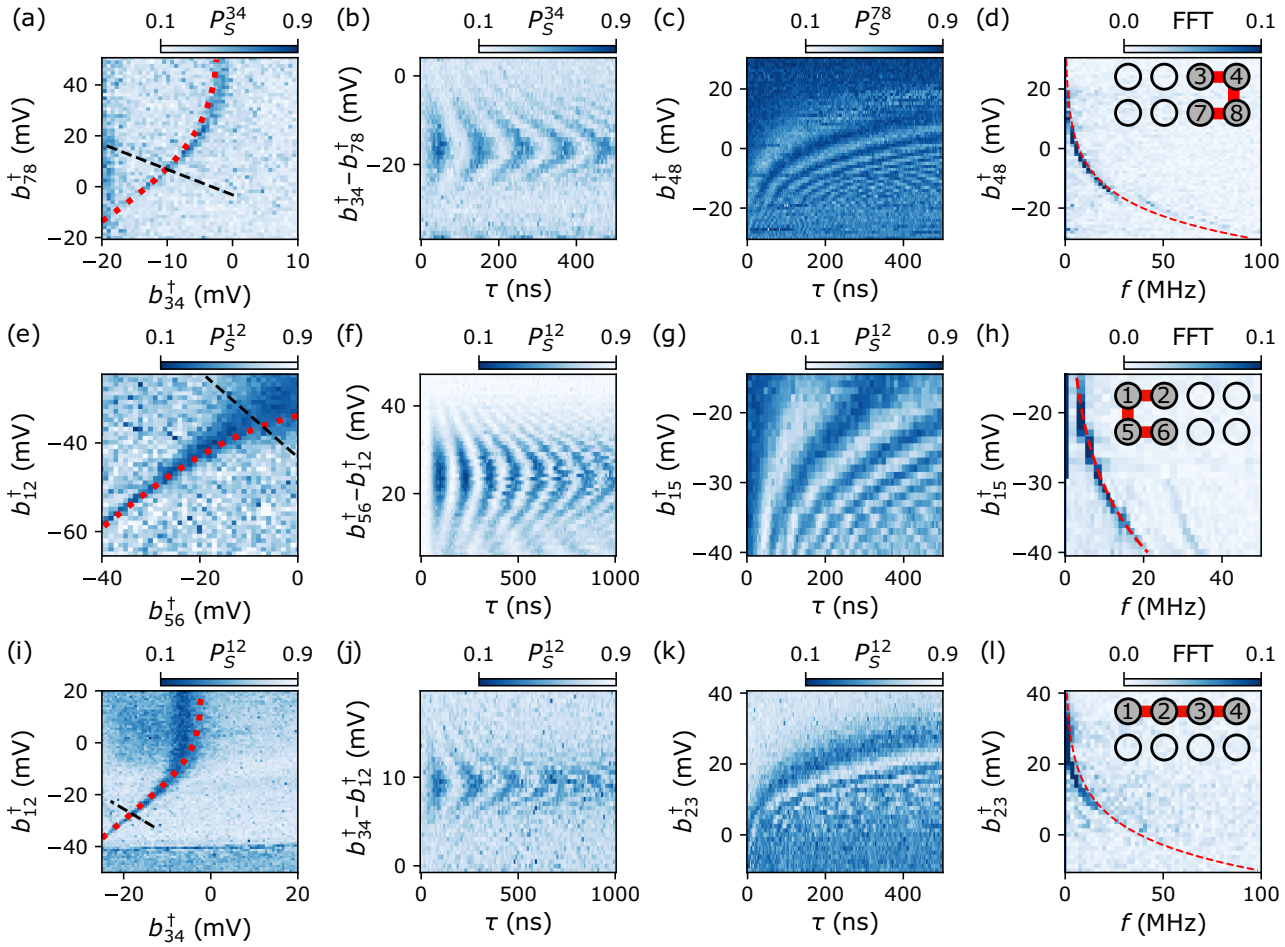

FIG. 5. (a) Resonant $|S_{78}T_{34}^-\rangle \leftrightarrow |T_{78}^-S_{34}\rangle$ condition as a function of $b_{34}^\dagger$ and $b_{78}^\dagger$ with exchange $J_{48} \approx 2$ MHz induced by $b_{48}^\dagger$. We record the probability of measuring $|S_{34}\rangle$ after initializing $|S_{78}T_{34}^-\rangle$ and letting the system evolve for $\tau = 380$ ns, corresponding to a near perfect inversion of the population at the resonant condition marked by an increase in P_S^{34}. The red dots mark the theoretical resonant condition, based on the Zeeman energies and individual exchange dependencies, which agrees well with the data. (b) Resonant $|S_{78}T_{34}^-\rangle \leftrightarrow |T_{78}^-S_{34}\rangle$ oscillations as a function of dwell time τ and $b_{34}^\dagger - b_{78}^\dagger$. The barriers are scanned along the dashed line in (a). The maximum oscillation amplitude corresponds to the resonant condition, and the frequency $hf = J_{48}$. (c) Resonant $|S_{78}T_{34}^-\rangle \leftrightarrow |T_{78}^-S_{34}\rangle$ oscillations as a function of dwell time τ and $b_{48}^\dagger$ at the resonant condition. (d) FFT of (c). The dashed red line is the exchange dependence $J_{48}(b_{48}^\dagger)$ extracted from the isolated Q_{48} oscillations, which matches well with the observed FFT peak. The latter yields $J_{48}(b_{48}^\dagger)$ with the two neighboring exchanges activated. The inset shows a sketch of the quantum dots and interactions involved in the experiments reported in (a)–(d). (e)–(h) Similar to (a)–(d) but for the chain 2-1-5-6. In this case $b_{15}^\dagger$ was not virtualized due to the rather small crosstalk elements. (g),(h) Data pertaining to the resonant $|S_{12}T_{34}^0\rangle \leftrightarrow |T_{12}^0S_{34}\rangle$ condition. The dashed red line in (h) is a fit and allows us to extract $J_{15}(b_{15}^\dagger)$ even without complete virtualization. (i)–(l) Similar to (a)–(d) but for the chain 1-2-3-4. While we find good agreement with the predicted resonant condition in (i), the oscillation frequency in (j),(k) is different from the expected value extracted from the isolated Q_{23} oscillations. We find good agreement with the data if we correct the value of $b_{0,23}^\dagger$ by -6 mV. This suggests that some residual, possibly nonlinear, crosstalk remains, which will require more sophisticated mitigation strategies to account for it.

Finally, in Fig. 5(c) we report coherent $|S_{78}T_{34}^-\rangle \leftrightarrow |T_{78}^-S_{34}\rangle$ oscillations as a function of $b_{48}^\dagger$ at the resonant condition, while recording P_S^{78} this time. Figure 5(d) shows the FFT of Fig. 5(c), and the dashed red line is the exchange dependence $J_{48}(b_{48}^\dagger)$ we extracted from the isolated Q_{48} measurements. Since also here we find good agreement, we conclude that, in this case, the virtualization of all three barrier gates involved was successful.

We repeat the same procedure for the chain 2-1-5-6 [Figs. 5(e)–5(h)]. Here we show data that were taken during a different cool-down and where $b_{15}^\dagger$ was not virtualized ($b_{12}^\dagger$ and $b_{56}^\dagger$ were virtualized). However, the crosstalk onto

$b_{15}^{\dagger}$ turned out to be relatively weak such that J_{15} was only mildly affected by $b_{12}^{\dagger}$ and $b_{56}^{\dagger}$. Moreover, Figs. 5(g) and 5(h) pertain to the resonant $|ST^0\rangle$ condition. The dashed red line in Fig. 5(h) is a fit to the data that allows us to extract $J_{15}(b_{15}^{\dagger})$ for this particular voltage configuration. In addition, in Fig. 22 in Appendix I we report further resonant condition plots similar to Fig. 5(f) for different values of $b_{15}^{\dagger}$ and observe that the position of the resonant condition does not change. We therefore conclude that the virtualization of $b_{12}^{\dagger}$ and $b_{56}^{\dagger}$ is correct also in this four-spin chain, and we have full knowledge of the Hamiltonian parameters in this configuration.

For the ultimate test, we consider the same plots as for the chain 3-4-8-7 also for the chain 1-2-3-4 involving b_{23}, which displays the severest crosstalk elements α_{23}^{mn}. [Figs. 5(i)–5(l)]. Although we find good theoretical agreement with the data in Fig. 5(i), to match the oscillation frequencies in Figs. 5(j) and 5(k), we needed to adjust the value of $b_{0,23}^{\dagger}$ by -6 mV compared with the values extracted via Eq. (3) from the isolated oscillations Q_{23}. This suggests that while we are able to correct for most of the crosstalk, there might be some nonlinear effects that we did not take into account. We have identified a possible cause of this, which was also extensively discussed in Ref. [8]. We observe nonlinear crosstalk between b'_{23} and p'_3, which we show in Fig. 8 in Appendix B. This can lead to miscalibrated crosstalk and the observed discrepancy between the isolated Q_{23} and the coupled four-spin chain measurement. To correct for such effects, we would require a more sophisticated, nonlinear crosstalk compensation scheme, which is beyond the scope of this work.

In general, we find that we are able to compensate most of the crosstalk and infer the Hamiltonian parameters also in the coupled four-spin chains. All the data are supported by numerical simulations that we report in Appendix I 1.

VI. DISCUSSION

In this work, we have proposed and demonstrated a way of directly extracting barrier-to-barrier crosstalk by tracking the constant-exchange feature given by the S-T^- avoided crossing in Ge. While the effects generally vary from gate to gate, we were able to observe a few trends. Electrodes featuring a fan-out in proximity to other gates typically display large crosstalk to other exchanges. For two-dimensional quantum dot arrays, these lateral fan-outs can be avoided through a vertical fan-out with vias [45–47]. Perfecting the gate layout and oxide composition can also contribute to reduced crosstalk, as demonstrated recently [10]. On the other hand, barrier gates oriented perpendicularly to each other and with no proximal fan-out typically show much less crosstalk, which seems easier to mitigate. This suggests that, for one-dimensional chains, a zigzag alignment of quantum dots could be favorable over a strictly linear placement.

An important verification tool in our work is the construction of four-spin chains and their time evolution at the resonant ST^- or ST^0 condition. It allowed us to confirm that the crosstalk extracted in the isolated two-qubit regime also mostly carries over to the regime of coupled four-spin chains. This important observation might enable the construction of longer spin chains with only local crosstalk calibration.

Finally, we emphasize also some of the limitations of this method. If we want to use the S-T^- avoided crossing, we can calibrate the crosstalk reliably in only the isolated two-spin regime and only for $J \approx E_{T^-}$. Other methods for direct crosstalk extraction can be used and also rely on following a constant-exchange feature, but are still limited to the isolated two-spin regime. For example, to extract the crosstalk elements α_{23}^{mn} we made use of exchange oscillations at a fixed time evolution (see Fig. 13 in Appendix D) as we did not calibrate $|S\rangle$ initialization and direct PSB readout due to the distance from the sensing quantum dots. This method is more versatile as it does not require spin-orbit interactions, making it suitable also for GaAs or silicon quantum dot devices. Nonetheless, we found that the S-T^- avoided crossing is a feature that is typically robust and easy to measure without knowledge of the particular Hamiltonian parameters such as the exchange dependence on any barrier or any lever arms. This information was crucial in earlier work on virtualization [5,6]. In practice, the method presented here is, therefore, preferable as it requires less overall knowledge of the device. These considerations make this method also a good candidate for automated calibrations [5,7], which can be easily integrated into existing routines [8].

With our findings, we have shed further light on the intricate crosstalk behavior in multilayered spin qubit devices. We also demonstrated that, despite the density of electrodes, linear crosstalk can be managed and corrected for. Generally, the designing of large spin-qubit arrays leaves room for improvement, for which this work provides valuable guidance. Furthermore, our results open the possibility of observing multispin physics in longer chains and two-dimensional geometries, with detailed knowledge of the underlying Hamiltonian [44].

ACKNOWLEDGMENTS

We thank M. Rimbach-Russ, T.-K. Hsiao, V. John, F. Borsoi, C.-A. Wang, and other members of the Vandersypen, Veldhorst, Scappucci, Rimbach-Russ, and Bosco groups for stimulating discussions. We acknowledge technical support by O. Benningshof, J. D. Mensingh, T. Orton, R. Schouten, R. Vermeulen, R. Birnholtz, E. Van der Wiel, B. Otto, and D. Brinkman. This work was funded by an Advanced Grant from the European Research

Council (ERC) under the European Union's Horizon 2020 research program (Grant No. 882848). We acknowledge support by the European Union through an ERC Starting Grant QUIST (Grant No. 850641). We acknowledge support by the Army Research Office under Grant No. W911NF2310110.

The views and conclusions contained in this document are those of the authors and should not be interpreted as representing the official policies, either expressed or implied, of the Army Research Office or the U.S. Government. The U.S. Government is authorized to reproduce and distribute reprints for government purposes notwithstanding any copyright notation herein.

DATA AVAILABILITY

The data that support the findings of this article are openly available [48].

APPENDIX A: DEVICE FABRICATION AND EXPERIMENTAL SETUP

The device is fabricated on a $Ge/Si_{0.2}Ge_{0.8}$ heterostructure with a quantum well buried 55 nm below the surface. The growth is performed by chemical vapor deposition starting from a Si substrate. After growth of a thick layer of Ge on the substrate, the Si concentration is linearly increased to reach the desired composition [Fig. 6(e)] [29]. The fabrication starts with markers and SiN pads patterned via optical lithography. Subsequently, the Ohmic contacts are defined via electron-beam lithography [Fig. 6(a)]. The

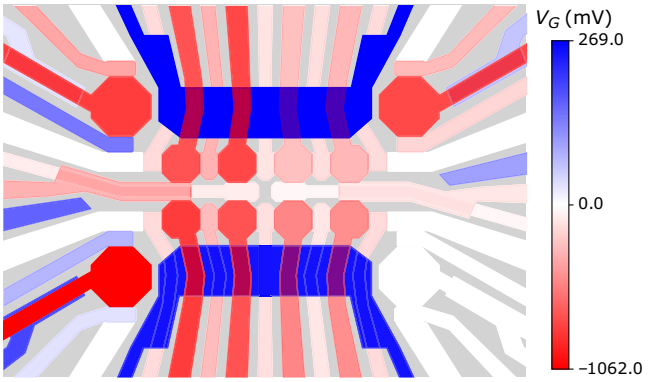

FIG. 7. Typical dc voltage configuration in the experiments presented in this work. The color scale reflects the voltage V_G applied to the individual electrodes. Electrodes in white are either grounded or have 0 V applied. All voltages on the bottom-right sensor are 0 V as the sensor plunger was faulty. Starting from the dc configuration, pulses on the AWG channels allow us to quickly change the charge state or the exchange.

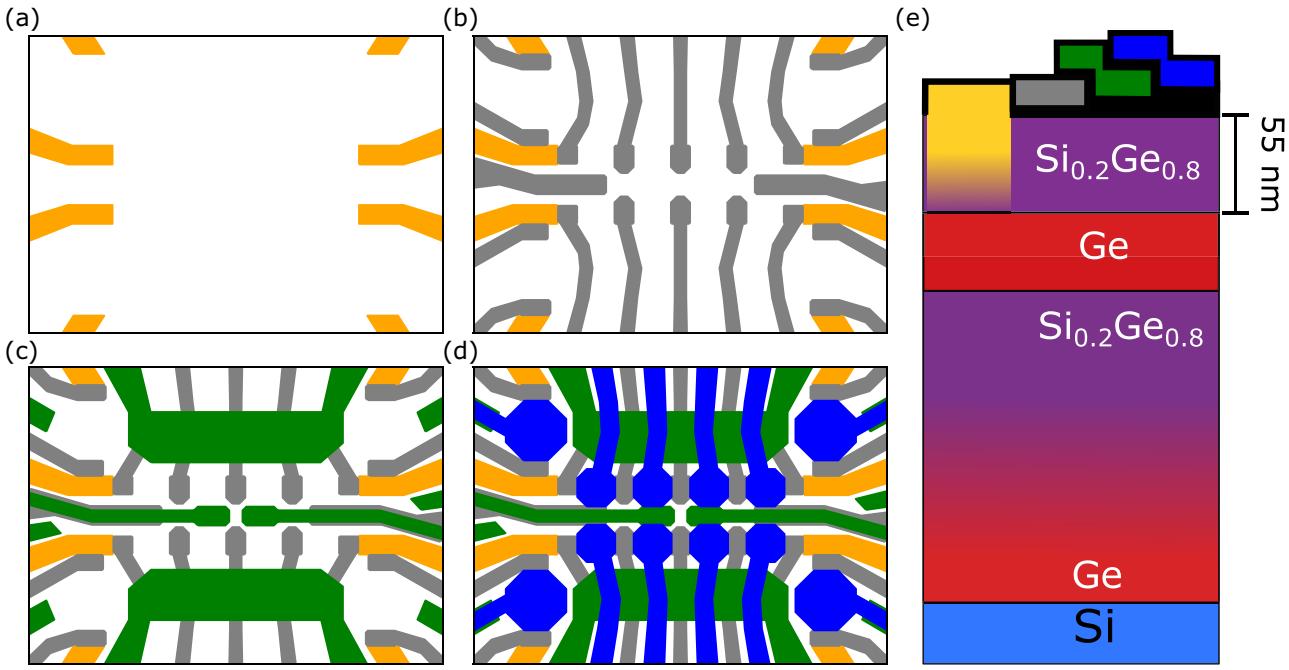

FIG. 6. Device design and heterostructure. (a) In the first metal layer we deposit the Ohmic contacts. (b) After annealing while depositing the gate oxide, we proceed with the first barrier gate layer, which also includes the sensor barriers to the leads. (c) In the third gate layer, we deposit screening gates and the two central barrier gates b_{26} and b_{37}. (d) Finally, we deposit the plunger gates including the sensors. (e) Heterostructure with the gate stack on top. The thick black layers in between the gates symbolize the gate oxides.

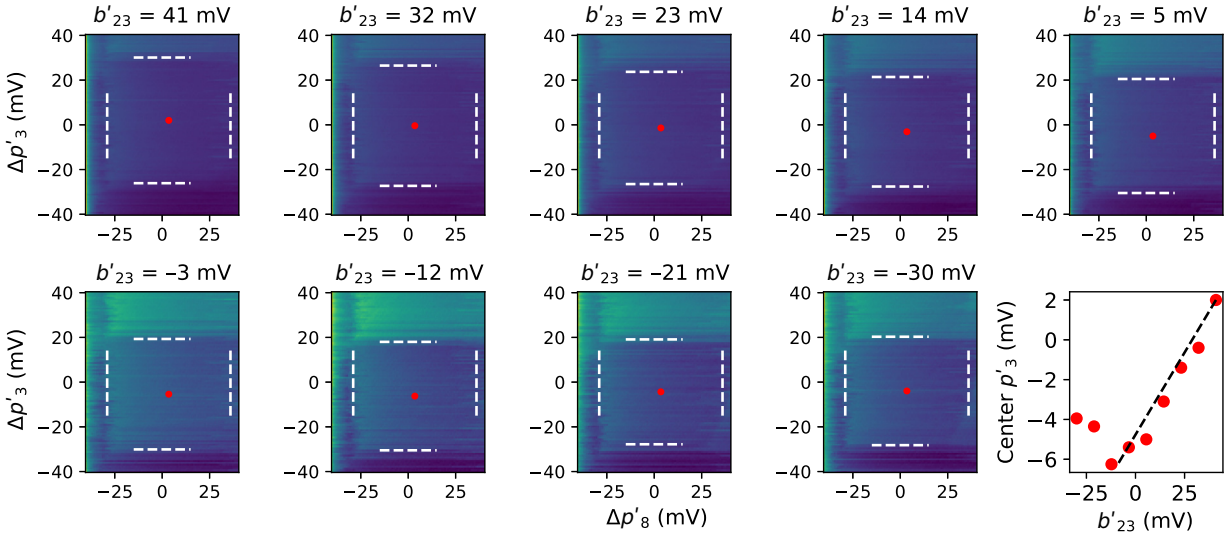

FIG. 8. Plunger against barrier virtualization. The plots show charge stability diagrams of p'_8 vs p'_3 while b'_{23} is changed. The dashed white lines mark the charge transitions of quantum dot 8 (vertical) and quantum dot 3 (horizontal). The red dot is the center of the charge stability region, which we can follow in all the plots as we lower the value of b'_{23}. The panel at the bottom right shows the extracted center position of p'_3 for the different barrier voltages. The dashed black line allows us to extract the crosstalk correction between b'_{23} and p'_3. However, we notice that for very negative barrier voltages the center position deviates from this line, indicating that the crosstalk has changed. Similar observations were made in Ref. [8] and will require more sophisticated nonlinear correction schemes.

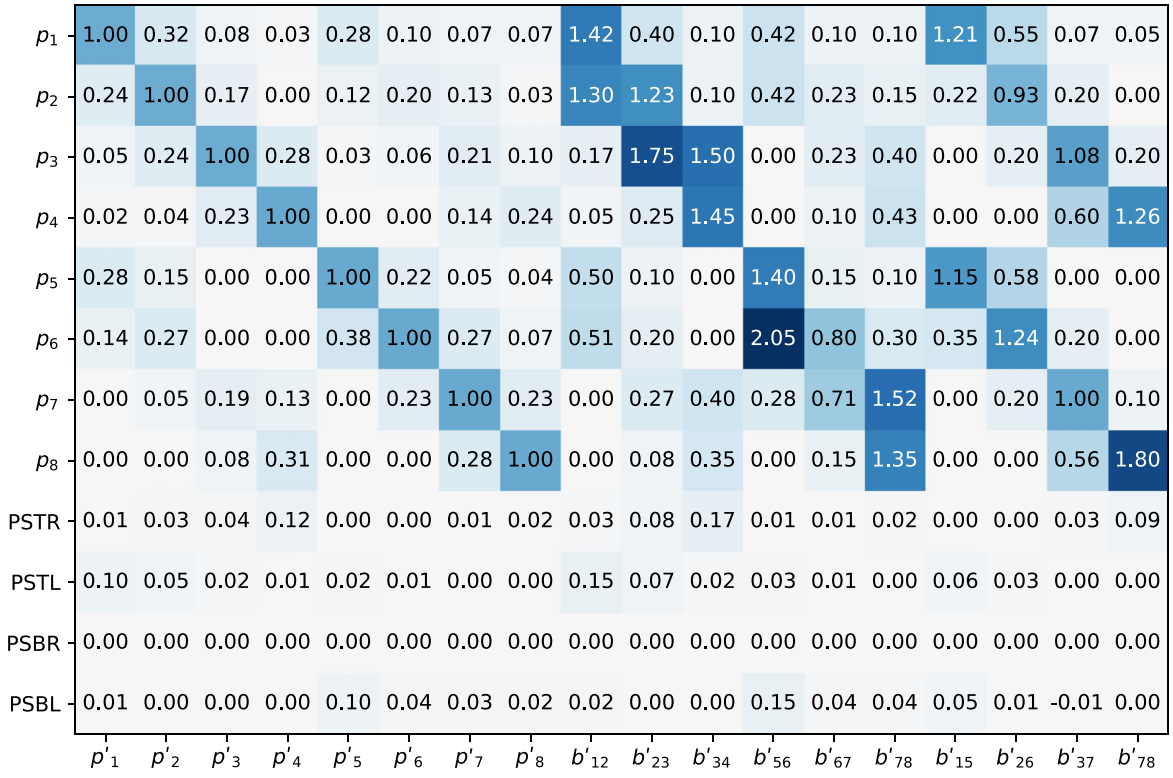

FIG. 9. Crosstalk matrix for a first layer of gate virtualization. The linear combination of p_i and b_{ij} to orthogonally control the quantum dot potentials is obtained from the inverse of this matrix. As a consequence of deposition of the barrier gates as a first gate layer, large correction pulses on the plungers are needed to compensate for barrier pulses, as highlighted by the large crosstalk elements. For example, a pulse on b'_{56} would require a pulse of twice the amplitude on p_6 to maintain the electrochemical potential of quantum dot 6 unchanged. PSBL, plunger of the bottom-left sensor; PSBR, plunger of the bottom-right sensor; PSTL, plunger of the top-left sensor; PSTR, plunger of the top-right sensor.

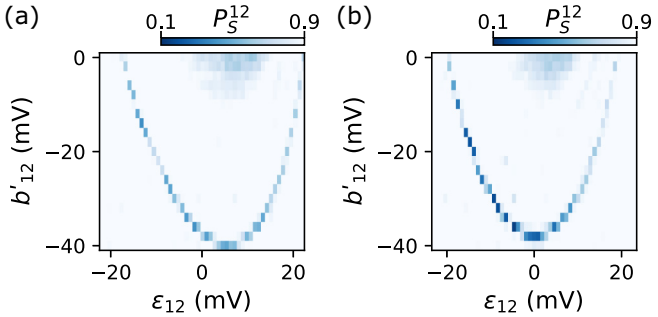

FIG. 10. (a) S-T^- avoided crossing of Q_{12} as a function of ϵ_{12} and b'_{12} with an improper first layer of virtualization leading to a skewed U shape. (b) Same measurement as in (a) but with corrected virtualization returning a symmetric U shape.

contact material is Pt, which, after deposition, is annealed during the oxide deposition (7 nm of Al_2O_3 grown by atomic layer deposition). In the following, we alternate electron-beam lithography, metal deposition, and oxide growth to define the barrier gate layer [Fig. 6(b)], the screening gate layer [Fig. 6(c)], and the plunger gate layer [Fig. 6(d)]. The gate material is Ti/Pd, with a thickness of 3 and 17 nm, respectively, for the first gate layer, 3 and 27 nm, respectively, for the second gate layer, and 3 and 37 nm, respectively, for the third gate layer.

All measurements are performed in an Oxford Triton dilution refrigerator at a nominal base temperature of 13 mK. We apply magnetic fields of 10 mT in the in-plane direction. The device is mounted on a custom-made printed circuit board (PCB). dc voltages from homebuilt serial peripheral interface digital-to-analog converter modules and pulses from a Keysight M3202A arbitrary waveform generator are combined with the use of on-PCB bias tees. Radio-frequency reflectometry for charge sensing is done with the use of serial peripheral interface in-phase and quadrature demodulation modules and on-PCB LC tank circuits. The demodulated signals are recorded by a Keysight M3102A digitizer.

The voltages necessary to tune the device into a regime with a single hole in each of the eight quantum dots (except quantum dot 2, where three holes are confined) and form single-hole transistors in the top-left, top-right, and bottom-left quantum dots are plotted as a heat map in Fig. 7. We found that the bottom-right sensor was faulty, which is why all voltages in that area are set to 0 V.

APPENDIX B: CROSSTALK MATRIX FOR PLUNGER VIRTUALIZATION

Virtual plunger gates ease device control and are rather straightforward to obtain from charge stability diagrams. Plunger-to-plunger crosstalk can be directly extracted from the slopes of the reservoir addition lines. To compensate for crosstalk from barriers to plungers it is important to account for the fact that increased coupling, induced by the barrier, will also modify the plunger-to-plunger crosstalk element. We must therefore ensure we first start from a set of dc gate voltages close to the desired operating conditions. Once a suitable dc voltage configuration is found, we record charge stability diagrams and change the barriers in steps. In this way, it is possible to track the center of the (1,1) charge stability region as a function of the barrier and compensate for this shift (we use a manual version of the method described in Ref. [8]) (Fig. 8). The resulting virtual gate matrix is depicted in Fig. 9.

In a next step, we define detunings $\epsilon_{ij} = ap'_j - bp'_i$ and electrochemical potentials $\mu_{ij} = cp'_j + dp'_i$ where a, b, c, and d are coefficients that we experimentally determine.

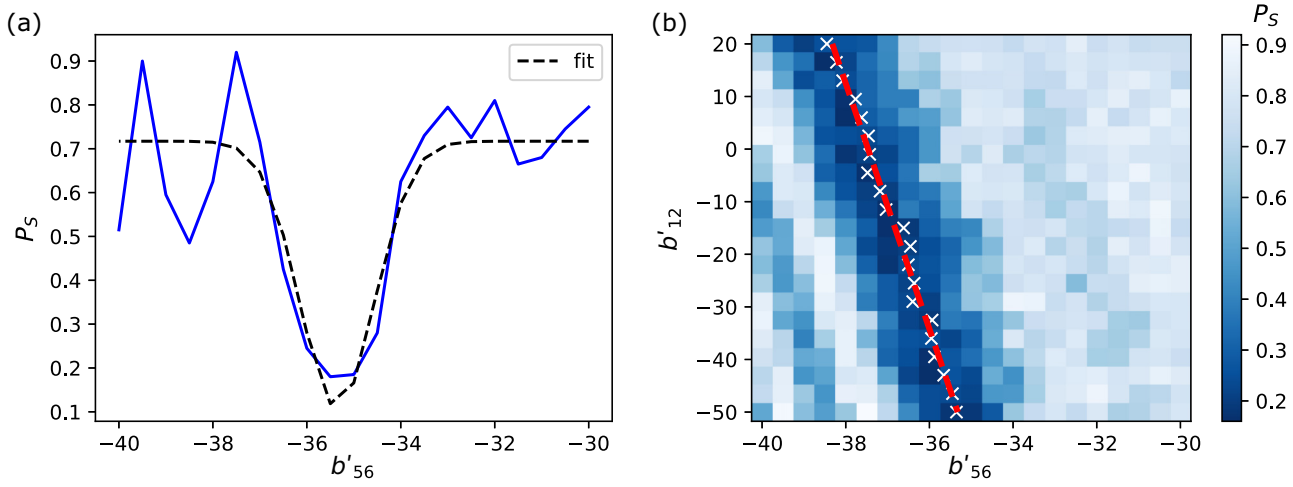

FIG. 11. (a) Line-cut of (b) corresponding to the top-right panel in Fig. 3. (a) We fit a Gaussian to the data to extract the position of the minimum in the singlet probability. We repeat this for every value of b'_{12}. (b) Crosstalk extraction α^{12}_{56}. The white crosses are the extracted minima in P_S. The dashed red line is a fit to the data. The slope returns $-\alpha^{12}_{56}$.

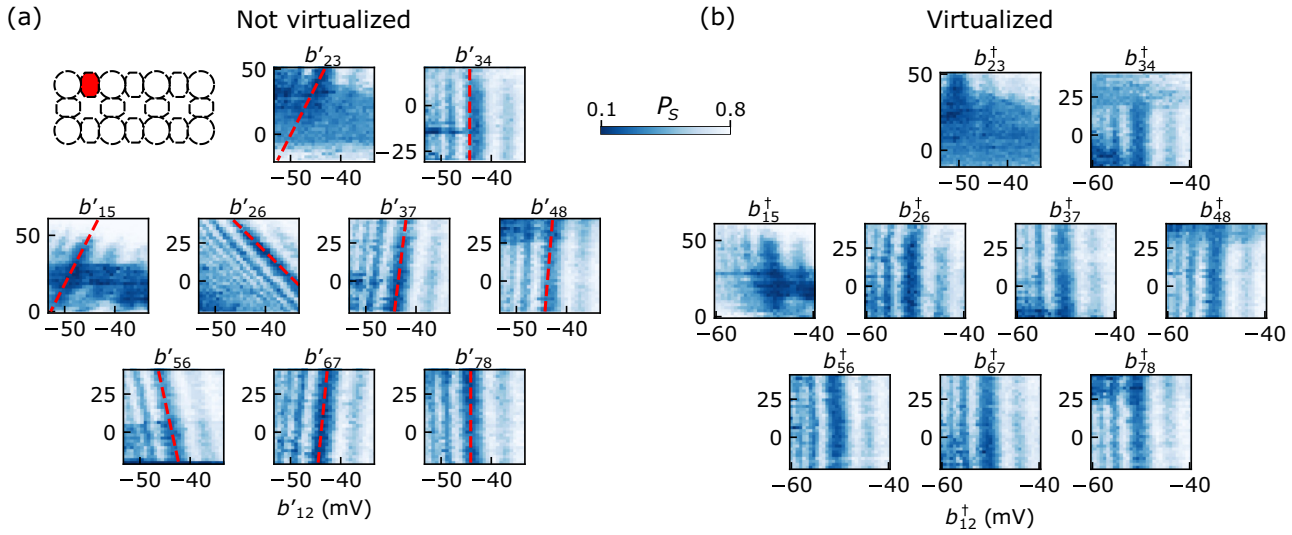

FIG. 12. (a) S-T^- avoided crossing of Q_{12} as a function of b'_{12} and all the other barriers b'_{ij}. The slopes return the crosstalk element α^{mn}_{12}. (b) S-T^- avoided crossing of Q_{12} as a function of $b^\dagger_{12}$ and all the other virtual barriers $b^\dagger_{ij}$.

If the definitions of ϵ_{ij} and the barrier-to-plunger virtualization are correct, the S-T^- avoided crossing position as a function of detuning and (virtual) barrier should be a symmetric U shape (in the absence of modulations of the g factor) [32]. An example of an ill-defined virtualization leading to a skewed U shape is depicted in Fig. 10(a), while Fig. 10(b) shows the same measurement with corrected virtualizations. This step is crucial for the subsequent barrier-to-barrier compensation, since an unwanted detuning between the quantum dots would enhance the exchange of interest.

APPENDIX C: CROSSTALK EXTRACTION

Figure 11 shows the process for extracting the crosstalk element. In Fig. 11(a) we show a line-cut of the top-left panel of Fig. 3. The dashed black line is a Gaussian fit from which we are able to extract the position of the

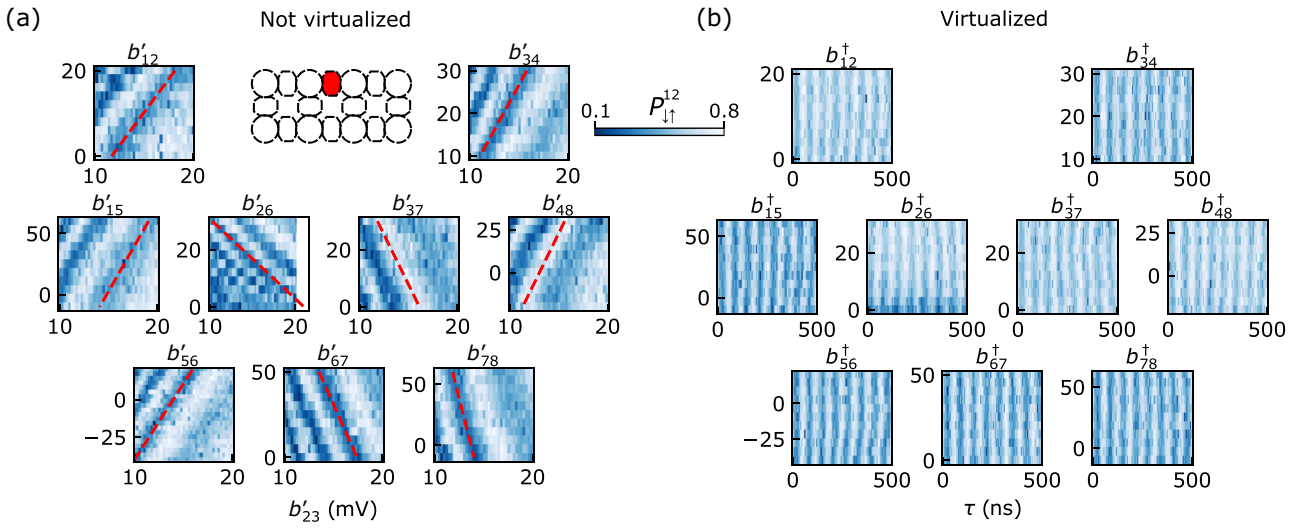

FIG. 13. (a) Exchange oscillations of Q_{12} as a function of b'_{23} and all the other barriers b'_{ij}. Since we do not have direct access to the S-T^- avoided crossing in Q_{23}, we opted to initialize $|\downarrow\uparrow\downarrow\downarrow\rangle$ in the top row and record $P^{12}_{\downarrow\uparrow}$. By fixing the evolution time τ and scanning b'_{23} against the other barriers, we are still able to follow features and extract the crosstalk element, although no feature stands out more than others. (b) Exchange oscillations of Q_{12} as a function of $b^\dagger_{mn}$ and duration τ. None of the virtual barriers $b^\dagger_{ij}$ affect the oscillation frequency, which indicates that the crosstalk to $b^\dagger_{23}$ is correctly compensated.

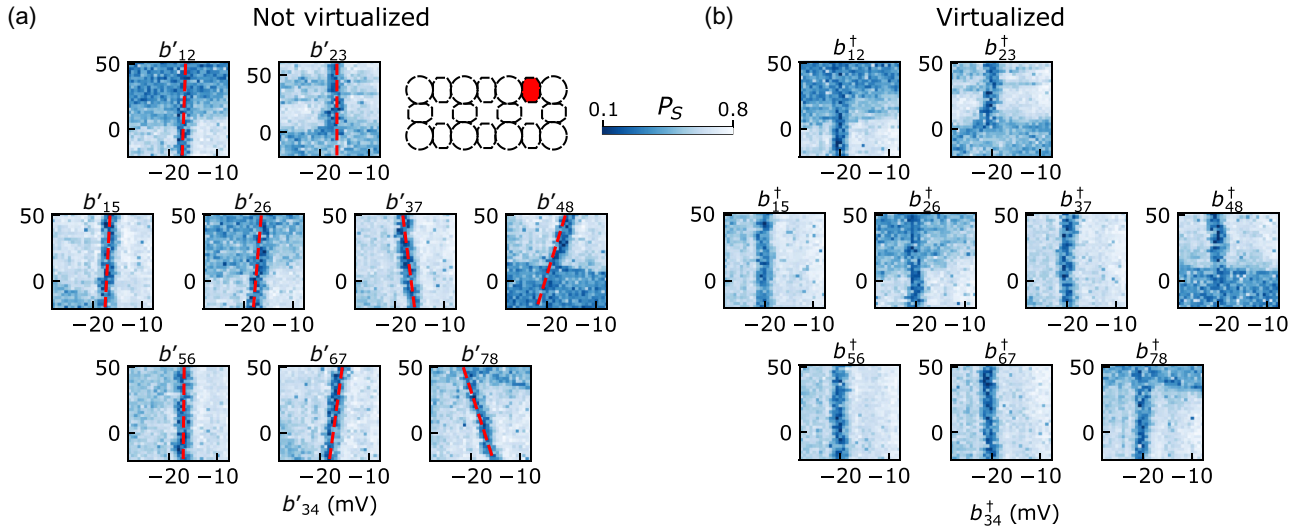

FIG. 14. (a) S-T^- avoided crossing of Q_{34} as a function of b'_{34} and all the other barriers b'_{ij}. The slopes return the crosstalk element α^{mn}_{34}. (b) S-T^- avoided crossing of Q_{34} as a function of $b^\dagger_{34}$ and all the other virtual barriers $b^\dagger_{ij}$.

avoided crossing. The white crosses in Fig. 11(b) mark the extracted avoided crossing positions, to which we can fit the dashed red line. The crosstalk element α^{12}_{56} is simply the slope multiplied by -1. Such a procedure is repeated for all the other barrier gates to fill out the crosstalk matrix.

APPENDIX D: CROSSTALK FOR OTHER BARRIERS

Figures 12–17 present data analogous to the data shown in Fig. 9 for Q_{56}. Specifically, they show the avoided crossing features or exchange oscillations of Q_{12}, Q_{23}, Q_{34}, Q_{15}, Q_{48}, and Q_{78}, respectively. In Figs. 12–17, the plots associated with the respective barriers are organized to reflect the geometry of the device. We always chose the ranges in a way to not induce any exchange for nearest-neighbor barriers. For Q_{23} we do not have access to direct PSB readout. Therefore, we opted to initialize the state $|\downarrow\uparrow\downarrow\downarrow\rangle$ in the top row and record exchange oscillations at a fixed duration τ and scan b'_{23} against b'_{mn}. We record the probability $P^{12}_{\downarrow\uparrow}$, which, with b'_{12} and b'_{34} not inducing any exchange, oscillates at a frequency determined by b'_{23}. While the resulting features are not as clear and isolated as

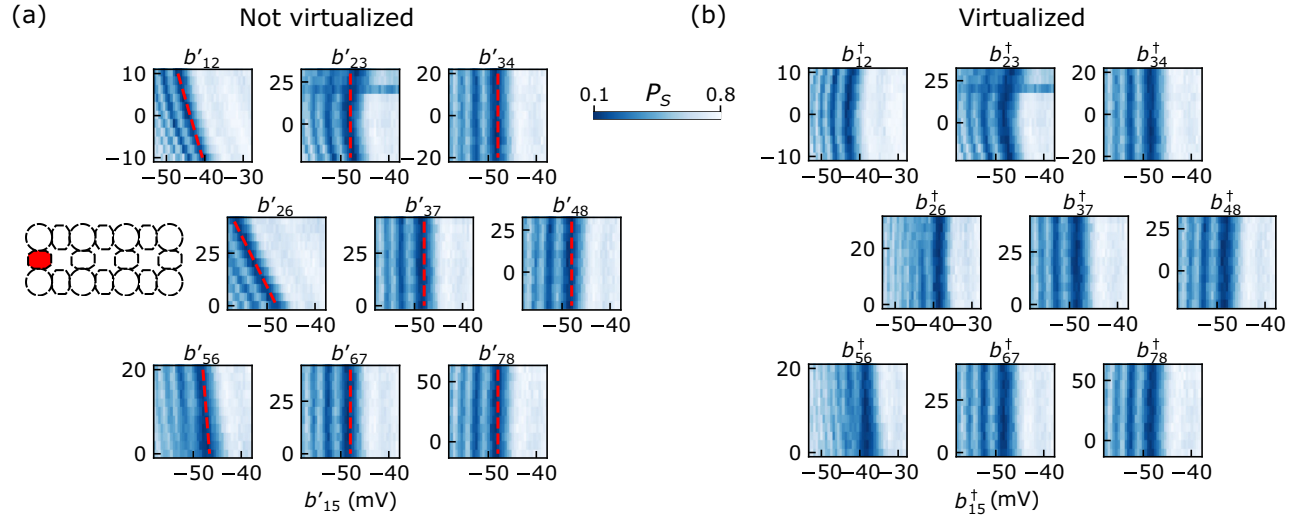

FIG. 15. (a) S-T^- avoided crossing of Q_{15} as a function of b'_{15} and all the other barriers b'_{ij}. The slopes return the crosstalk element α^{mn}_{15}. (b) S-T^- avoided crossing of Q_{15} as a function of $b^\dagger_{15}$ and all the other virtual barriers $b^\dagger_{ij}$. Except for $b^\dagger_{23}$ all the virtualizations are correct. We note that when a gate crosstalk element is zero, $b'_{mn} = b^\dagger_{mn}$ for this case and we simply reproduced the plots from (a) in (b).

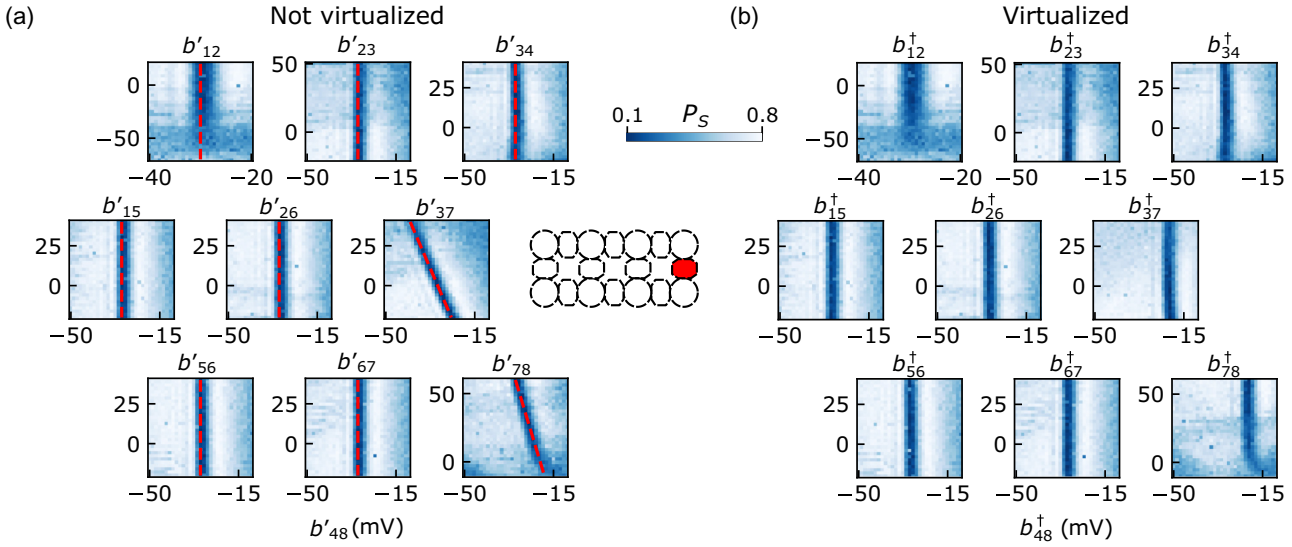

FIG. 16. (a) S-T^- avoided crossing of Q_{48} as a function of b'_{48} and all the other barriers b'_{ij}. The slopes return the crosstalk element α^{mn}_{48}. (b) S-T^- avoided crossing of Q_{48} as a function of $b^\dagger_{48}$ and all the other virtual barriers $b^\dagger_{ij}$. We note that when a gate crosstalk element is zero, $b'_{mn} = b^\dagger_{mn}$ for this case and we simply reproduced the plots from (a) in (b).

the ones from the avoided crossing, they still allow us to extract a crosstalk element. Figure 13(b) shows exchange oscillations between spins 2 and 3, again recorded as $P^{12}_{\downarrow\uparrow}$, which are not influenced by any of the $b^\dagger_{mn}$, demonstrating that crosstalk is compensated.

Lastly, we note that the crosstalk elements reported in Fig. 4(b) are the ones we used in the experiments reported in Fig. 5 and are not necessarily the same as the slopes in the measurements here would suggest.

APPENDIX E: INITIALIZATION AND READOUT SCHEMES

Figure 18 schematically shows the different initialization and readout schemes. A fast pulse [Fig. 18(c)] initializes and reads $|S\rangle$, a ramped pulse starting after the avoided crossing [Fig. 18(e)] initializes $|\downarrow\uparrow\rangle$ or $|\uparrow\downarrow\rangle$, while a ramped pulse starting before the avoided crossing initializes $|\downarrow\downarrow\rangle$. During the time evolution in (1,1) we apply a pulse on a barrier to induce exchange. Combining the initialization pulse with an appropriate pulse shape to

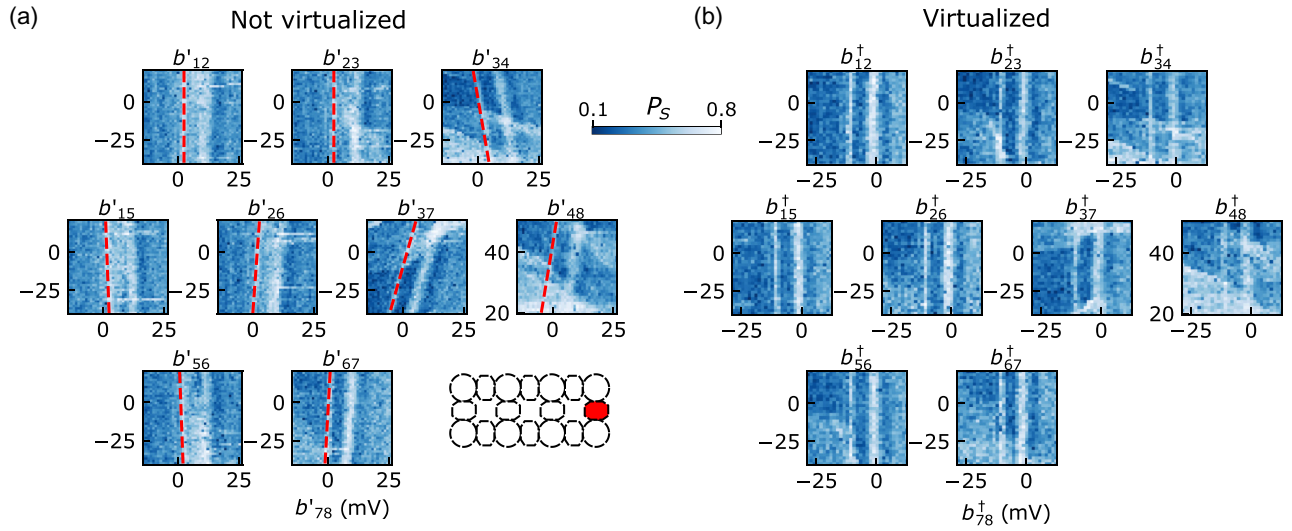

FIG. 17. (a) S-T^- avoided crossing of Q_{78} as a function of b'_{78} and all the other barriers b'_{ij}. The slopes return the crosstalk element α^{mn}_{78}. (b) S-T^- avoided crossing of Q_{78} as a function of $b^\dagger_{78}$ and all the other virtual barriers $b^\dagger_{ij}$.

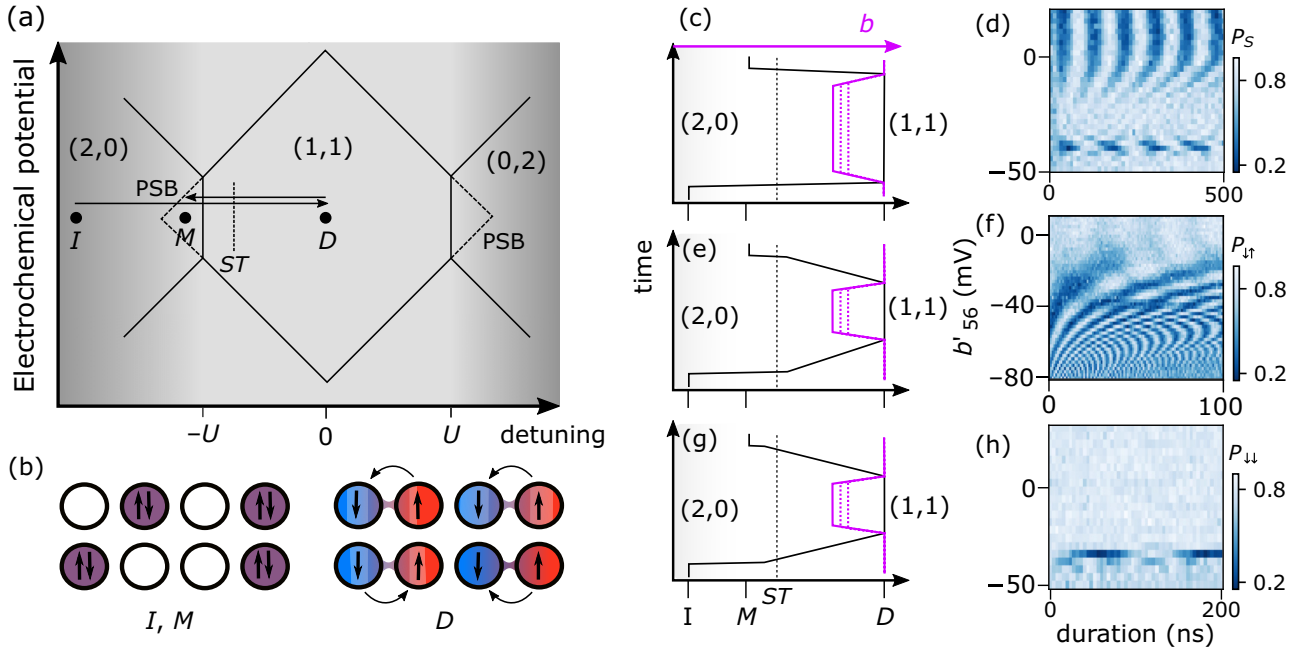

FIG. 18. (a) Charge stability diagram of a double quantum dot as a function of detuning and the electrochemical potentials of the two quantum dots, which are uniformly varied. When the detuning is equal to the charging energy U, charges are transferred between the quantum dots through the vertical transition lines. The region inside the dashed triangle corresponds to the metastable region, where Pauli spin blockade occurs, assuming the triplet excited state falls outside the triangle (otherwise the triangle is truncated). A typical experiment starts with two charges in one of the two quantum dots [(2,0) or (0,2) charge region, as depicted in the left sketch in (b)]. We then pulse the system into the (1,1) region at the dwell point D. Depending on the ramp type [(c), (e), or (g)] we initialize $|S\rangle$, $|\downarrow\uparrow\rangle$, or $|\downarrow\downarrow\rangle$. After letting the system evolve, we pulse the detuning back to the measurement point M and perform single-shot readout of the final state. (b) Typical charge and spin configuration at the initialization point I and measurement point M (left) as well as at the dwell point D (right). (c) Pulse scheme to obtain ST^0 oscillations for initialization in $|S\rangle$ and reading $|S\rangle$ (by "reading a state," we mean distinguishing this state from the other three states in the two-qubit space). After pulsing the detuning quickly to D, we diabatically pulse on the barrier voltage and next diabatically pulse the detuning back to M. A typical oscillation pattern as in (d) emerges. (d) Singlet-triplet oscillations of Q_{56} as a function of b'_{56}. For more positive barrier voltages we clearly see S-T^0 oscillations at frequency $hf = \Delta g_{56}\mu_B B$. As the barrier voltage is lowered and exchange increases, the oscillation frequency increases and the visibility is lowered, indicating the initial $|S\rangle$ state is now an eigenstate of the system. Around $b'_{56} = -40$ mV another oscillation can be observed, corresponding to S-T^- oscillations at the S-T^- avoided crossing. (e) Pulse scheme to obtain exchange oscillations for initialization and readout of $|\uparrow\downarrow\rangle$. By ramping the detuning adiabatically with respect to $\Delta g\mu_B B$ (after diabatically sweeping over the S-T^- avoided crossing), we are able to initialize an antiparallel spin state at the dwell point. A diabatic pulse on the barrier will then induce SWAP oscillations between $|\uparrow\downarrow\rangle$ and $|\downarrow\uparrow\rangle$. Ramping the detuning back adiabatically until the avoided crossing and then diabatically until the measurement point takes the final $|\uparrow\downarrow\rangle$ state onto a singlet (2,0) during readout, effectively returning $P_{\uparrow\downarrow}$. (f) Exchange oscillations as a function of b'_{56} with use of the pulse scheme in (e). This time we see the amplitude of the oscillations increase as we lower the barrier voltage and exchange is enhanced, as expected for SWAP oscillations starting from $|\downarrow\uparrow\rangle$. (g) Pulse scheme to obtain oscillations for initialization and reading $|T^-\rangle$ by adiabatically ramping the detuning over the S-T^- avoided crossing. The same adiabatic ramp before readout takes $|T^-\rangle$ onto a singlet (2,0) during readout, effectively returning $P_{\downarrow\downarrow}$. Between initialization and readout, a diabatic barrier pulse is applied. (h) With the pulse scheme in (g) we now see oscillations only at the S-T^- avoided crossing as expected when starting from $|T^-\rangle$.

the readout point unveils ST^0 oscillations [Fig. 18(d)], exchange oscillations [Fig. 18(f)], or ST^- oscillations [Fig. 18(h)].

APPENDIX: F: *g* FACTORS

We extract the resonance frequencies f_i of our spins by means of electric dipole spin resonance and find our effective g factors as $g_i = \frac{f_i}{\mu_B B}h$, where h is Plank's constant, at field $B = 10$ mT. The results are summarized in Fig. 19.

APPENDIX G: EXCHANGE PROFILES FOR BARRIER GATES

We typically operate every singlet-triplet qubit at its symmetry point ($\epsilon_{ij} = 0$). Here the exchange is determined solely by the height of the tunnel barrier ($J = \frac{2t^2}{U}$). It is common practice to approximate the exchange dependence on the barrier by an exponential function $J(b_{ij}) = J_0 \exp\left(k(b_{ij} - b_{0,ij})\right)$, where $b_{0,ij}$ is an offset determined by the dc voltage configuration and $J_0 = 1$ MHz. k can be

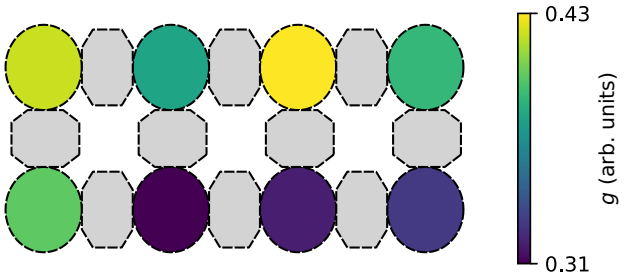

FIG. 19. g factors for the spins in the different quantum dots. The g factors were extracted from electric dipole spin resonance experiments (data not shown).

interpreted as a barrier lever arm, e.g., how strongly the barrier voltage affects the exchange. This is dependent on the gate layout and the dc voltage configuration. Figure 20 shows the exchange profiles of the singlet triplet qubits we measured alongside their FFTs and fits to the exchange formula. Table I summarizes the extracted values for all the singlet-triplet qubits measured.

APPENDIX H: SINGLET-TRIPLET RESONANT CONDITIONS

In this appendix we further elucidate the reasoning behind the resonant four-spin ST^{-} and ST^{0} conditions that

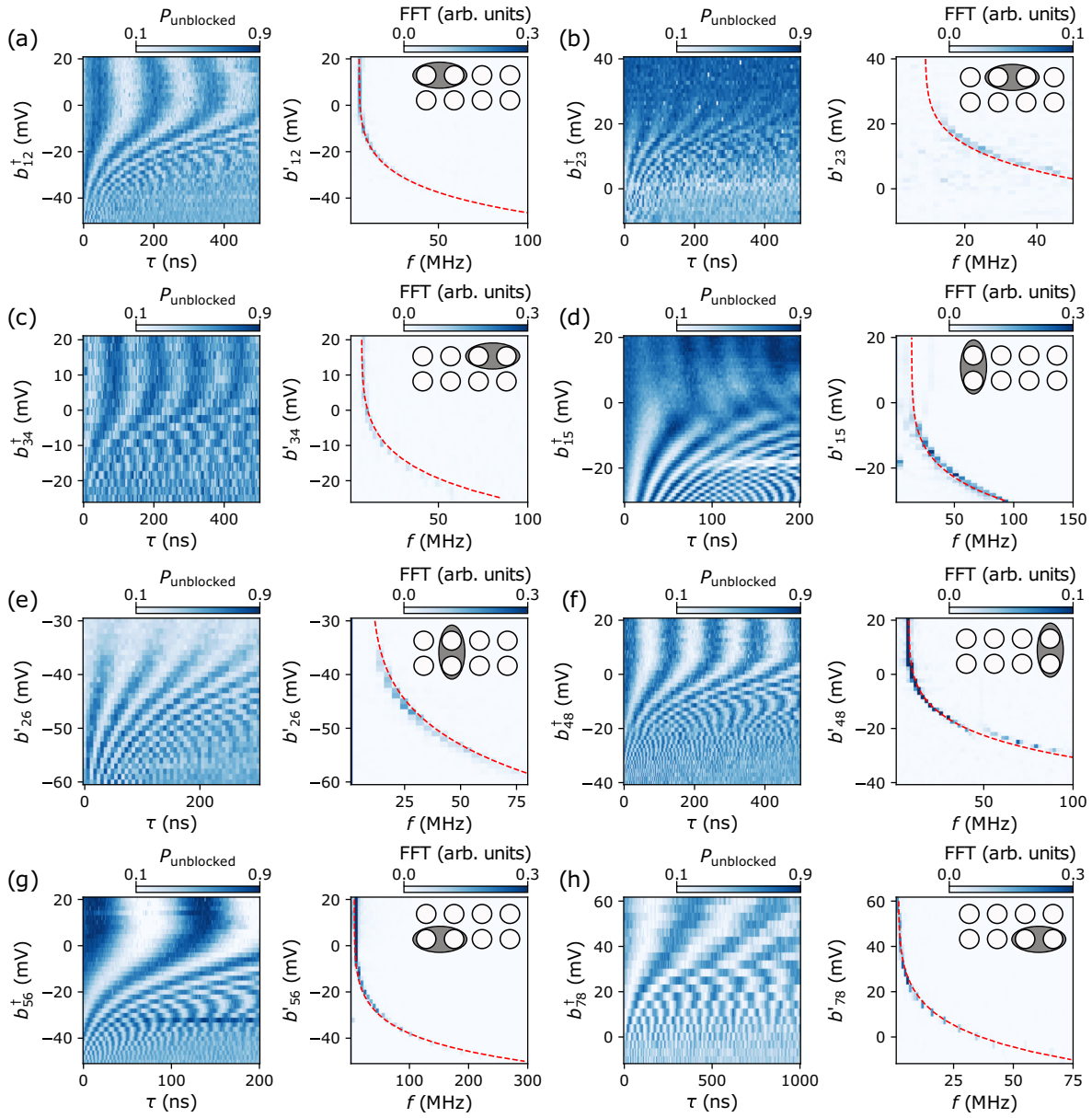

FIG. 20. (a)–(h) Exchange oscillations as a function of the barriers, and FFTs of the oscillations with fit to the exchange formula. The insets schematically show which S-T qubit is activated. All other exchanges are switched off.

TABLE I. Measured exchange dependencies on the barrier gates. b'_{37} and b'_{67} have not been measured, and b'_{26} is not virtualized. The dc voltages ensure that $|b^{\dagger}_{0,ij}| < 50$ mV, enabling a large on:off ratio within a comfortable pulse amplitude for the AWG. NM, not measured.

Gate	k (mV^{-1})	$b^{\dagger}_0$ (mV)
$b^{\dagger}_{12}$	−79.29	11.7
$b^{\dagger}_{23}$	−94.72	44.1
$b^{\dagger}_{34}$	−96.69	21.0
$b^{\dagger}_{15}$	−90.05	20.2
b'_{26}	−90.02	−9.8
b'_{37}	NM	NM
$b^{\dagger}_{48}$	−86.38	22.6
$b^{\dagger}_{56}$	−90.00	13.2
b'_{67}	NM	NM
$b^{\dagger}_{78}$	−71.6	50.1

are plotted in Fig. 5. In the presence of an external magnetic field B and isotropic but site-dependent g factors g_i, with $\hbar = 1$, the Heisenberg Hamiltonian assumes the form

$$H = \sum_i g_i \mu_B B S_{z,i} + \sum_i \Delta_{SO,i} S_{x,i} + \sum_{\langle i,j \rangle} J_{ij} \left(\mathbf{S}_i \mathbf{S}_j - \frac{1}{4} \right), \tag{H1}$$

TABLE II. Four-spin shared eigenstates of $\hat{S}^2$ and $\hat{S}^z$ expressed in a basis of two-spin singlets and triplets. As the Heisenberg Hamiltonian is spin conserving, it couples states only within the same subspace. Note that these states are, in general, not eigenstates of the Heisenberg Hamiltonian. The lowest two states of the T^0 and T^- subspace in the table are used to find resonant four-spin conditions in Fig. 5.

Subspace	(S, m_S)	Two-qubit basis states
	$(2, \pm 2)$	$\lvert T^{\pm}_{ij} T^{\pm}_{kl} \rangle$
Q	$(2, \pm 1)$	$\frac{1}{\sqrt{2}}(\lvert T^0_{ij} T^{\pm}_{kl} \rangle + \lvert T^{\pm}_{ij} T^0_{kl} \rangle)$
	$(2, 0)$	$\frac{1}{\sqrt{6}}(\lvert T^+_{ij} T^-_{kl} \rangle + \lvert T^-_{ij} T^+_{kl} \rangle + 2\lvert T^0_{ij} T^0_{kl} \rangle)$
$T^{\pm}$	$(1, \pm 1)$	$\frac{1}{\sqrt{2}}(\lvert T^0_{ij} T^{\pm}_{kl} \rangle - \lvert T^{\pm}_{ij} T^0_{kl} \rangle)$ $\lvert T_{ij \pm} S_{kl} \rangle$ $\lvert S_{ij} T^{\pm}_{kl} \rangle$
T^0	$(1, 0)$	$\frac{1}{\sqrt{2}}(\lvert T^+_{ij} T^-_{kl} \rangle - \lvert T^-_{ij} T^+_{kl} \rangle)$ $\lvert T^0_{ij} S_{kl} \rangle$ $\lvert S_{ij} T^0_{kl} \rangle$
S	$(0, 0)$	$\frac{1}{\sqrt{3}}(\lvert T^+_{ij} T^-_{kl} \rangle + \lvert T^-_{ij} T^+_{kl} \rangle - \lvert T^0_{ij} T^0_{kl} \rangle)$ $\lvert S_{ij} S_{kl} \rangle$

where $\mathbf{S} = (S_x, S_y, S_z)$ is the spin operator on site i. Here Δ_{SO} consists of anisotropic g-tensor components and the intrinsic spin-orbit interaction in the spin-orbit frame [49]. The influence of additional S_y terms in the spin-orbit term can be ignored if we analyze only the isolated ST^- (ST^0) subspace [32]. For four spins i, j, k, l it is instructive to write the basis states of the different spin subspaces in the familiar singlet-triplet basis of two-spin states. These are summarized in Table II. Without the spin-orbit interaction, a spin system initialized in one of these subspaces should evolve only within that subspace, e.g., the total spin number is conserved. We particularly want to draw attention to the two lowest states in the T^0 and T^- subspace. These states contain one singlet and one triplet each.

1. $|ST^-\rangle, |T^-S\rangle$ subspace

In the case of reduction to the basis $\left\{ |S_{ij} S_{kl}\rangle, |S_{ij} T^-_{kl}\rangle, |T^-_{ij} S_{kl}\rangle, |T^-_{ij} T^-_{kl}\rangle \right\}$ the Hamiltonian takes the form [32]

$$H_{ST^-} = \begin{pmatrix} -J_{ij} - J_{kl} & \frac{\Delta_{SO,kl}}{2} & \frac{\Delta_{SO,ij}}{2} & 0 \\ \frac{\Delta_{SO,kl}}{2} & -J_{ij} - \overline{E}_{z,kl} & -\frac{J_{jk}}{4} & \frac{\Delta_{SO,ij}}{2} \\ \frac{\Delta_{SO,ij}}{2} & -\frac{J_{jk}}{4} & -\overline{E}_{z,ij} - J_{kl} & \frac{\Delta_{SO,kl}}{2} \\ 0 & \frac{\Delta_{SO,ij}}{2} & \frac{\Delta_{SO,kl}}{2} & -2\overline{E}_{z,ijkl} + \frac{J_{jk}}{4} \end{pmatrix}. \tag{H2}$$

Compared with Eq. (2), we have included the spin-orbit part as well, which gives rise to leakage terms outside the $|S_{ij} T^-_{kl}\rangle, |T^-_{ij} S_{kl}\rangle$ subspace. However, these occur only at the respective avoided crossings ($J_{ij} = \overline{E_{Zij}}$), and it is easy to operate away from these locations. When $|J_{ij} - \overline{E}_{Z,ij}| = |J_{kl} - \overline{E}_{Z,kl}|$, the middle two diagonal terms are equal and the off-diagonal terms $\frac{J_{jk}}{4}$ become dominant. Initializing $|S_{ij} T^-_{kl}\rangle$ and pulsing quickly to this condition will induce $|S_{ij} T^-_{kl}\rangle \leftrightarrow |T^-_{ij} S_{kl}\rangle$ oscillations with frequency $f_{ST^-} = \frac{J_{jk}}{h}$ [26].

2. $|ST^0\rangle, |T^0S\rangle$ subspace

In the case of reduction to the basis $\left\{ |S_{ij} S_{kl}\rangle, |S_{ij} T^0_{kl}\rangle, |T^0_{ij} S_{kl}\rangle, |T^0_{ij} T^0_{kl}\rangle \right\}$ the Hamiltonian takes the form

$$H_{ST^0} = \begin{pmatrix} -J_{ij} - J_{kl} & \Delta E_{Z,kl} & \Delta E_{Z,ij} & -\frac{J_{jk}}{4} \\ \Delta E_{Z,kl} & -J_{ij} & -\frac{J_{jk}}{4} & \Delta E_{Z,ij} \\ \Delta E_{Z,ij} & -\frac{J_{jk}}{4} & -J_{kl} & \Delta E_{Z,kl} \\ -\frac{J_{jk}}{4} & \Delta E_{Z,ij} & \Delta E_{Z,kl} & 0 \end{pmatrix}.$$

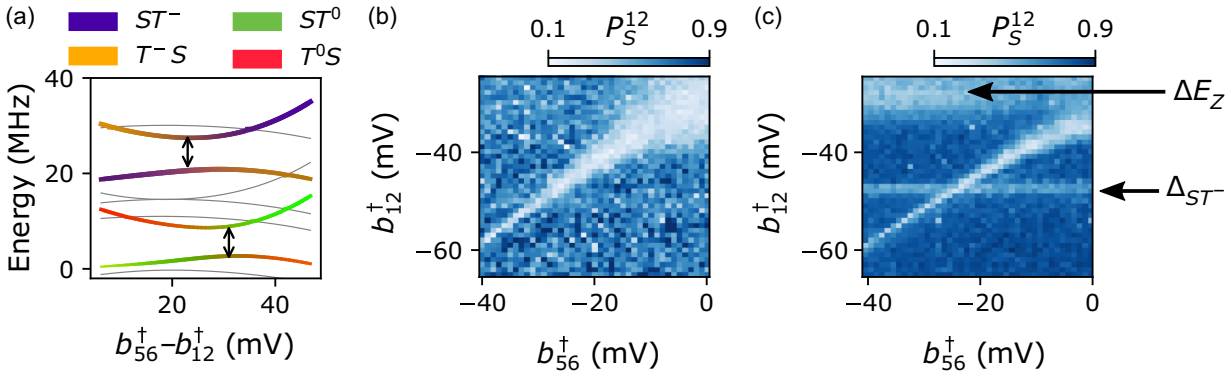

FIG. 21. (a) Simulated energy diagram of the four-spin system 2-1-5-6 as a function of $b^\dagger_{56} - b^\dagger_{12}$ as scanned in Fig. 5(b). The overlap with the four important states in the legend is color-coded and thickness-coded. We can observe two avoided crossings, one for $|ST^-\rangle \leftrightarrow |T^-S\rangle$ and the other for $|ST^0\rangle \leftrightarrow |T^0S\rangle$. The fact that the avoided crossings occur at different gate voltages reflects the slightly different requirements for J_{12} and J_{56}. However, the size of both avoided crossings is equal and determined solely by J_{15}. (b) Same as Fig. 5(e). (c) Resonant $|S_{12}T^0_{56}\rangle$ condition as a function of $b^\dagger_{56}$ and $b^\dagger_{12}$. We initialize $|S_{12}T^0_{56}\rangle$ and let the system evolve for 100 ns at each voltage point with a small exchange opened through $b^\dagger_{15}$. Like in (b) we can identify a sharp resonant condition that occurs at slightly different gate voltages than in (b) as $|S_{12}T^0_{56}\rangle$ evolves to $|T^0_{12}S_{56}\rangle$. In the bottom-left quadrant, however, the two resonant conditions approach each other. This is expected since J_{12} and J_{56} become the dominant energies in the system. We can also identify two leakage features indicated by the black arrows. One pertains to the singlet-triplet avoided crossing of Q_{12} (Δ_{SO}), while the other, at more positive voltages of $b^\dagger_{12}$, is attributed to ST^0 oscillations in Q_{12} since $J_{12} \approx \Delta E_{Z,12}$.

Similarly as in the case of the Hamiltonian (H2), we can identify a resonant condition: $\sqrt{J_{ij}^2 + \Delta E_{Z,ij}^2} = \sqrt{J_{kl}^2 + \Delta E_{Z,kl}^2}$. Again we find that at this special condition we can induce $|S_{ij}\,T^0_{kl}\rangle \leftrightarrow |T^0_{ij}\,S_{kl}\rangle$ oscillations at frequency $f_{ST^0} = \frac{J_{jk}}{h}$. In this case, however, the leakage terms outside this subspace are given by $\Delta E_{Z,ij,kl}$ and are slightly more difficult to avoid. We need to ensure that $J_{ij} \gg \Delta E_{Z,ij}$

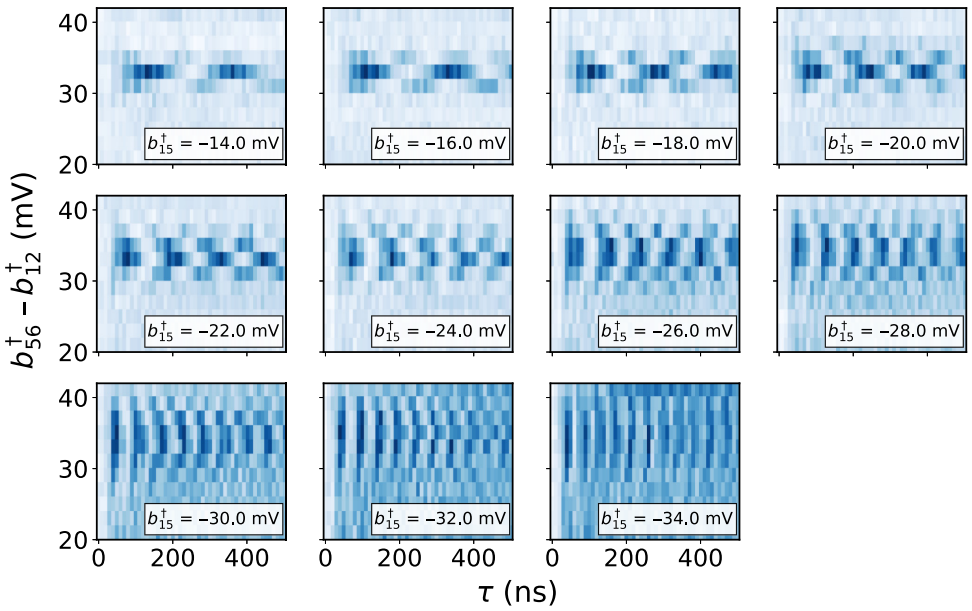

FIG. 22. Resonant $|S_{12}T^0_{56}\rangle$ condition. The color scale reflects the return probability P_S^{12} as in Fig. 5(b). We scan $b^\dagger_{56}$ from −7 to 3 mV while scanning $b^\dagger_{12}$ from −27 to −37 mV and changing $b^\dagger_{15}$ in steps. The resonant condition is marked by a maximum in the oscillation amplitude and a minimum in the oscillation frequency. We observe a stable position of the resonant condition as we decrease the voltage on $b^\dagger_{15}$, showing that J_{12} and J_{56} remain unaltered (or more specifically that $J_{56} - J_{12}$ remains unaltered). The chevron pattern we observe becomes broader as we decrease $b^\dagger_{15}$, which is expected as the off-diagonal term in the reduced four-spin Hamiltonian increases.

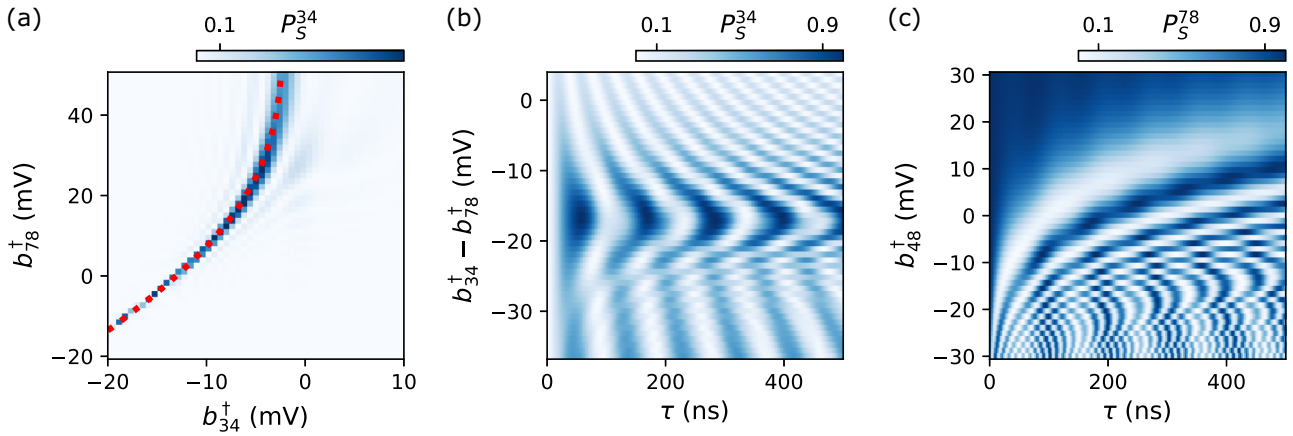

FIG. 23. Simulations of the chain spanned by quantum dots 3, 4, 8, and 7. (a) Simulated singlet return probability P_S^{34} as a function of $b_{34}^\dagger$ and $b_{78}^\dagger$ with an exchange opened between spins 4 and 8. The dotted red line is the same as in Fig. 5(a) and marks the condition $|J_{34} - E_{Z34}| = |J_{78} - E_{Z78}|$. We find excellent agreement with the data. (b) Resonant $S_{34}T_{78}^-$ condition. We sweep $b_{34}^\dagger$ and $b_{78}^\dagger$ like in the experiment reported in Fig. 5(b) and report P_S^{34}, finding again good agreement with the data. The leakage features for low values of $b_{34}^\dagger - b_{78}^\dagger$ are not prominent in the experiment, which we attribute to a low sensor contrast. (c) Resonant $S_{34}T_{78}^-$ oscillations as a function of $b_{48}^\dagger$ at the resonant ST^- condition. This time we report P_S^{78} as in the experiment. The simulation matches the experimental results in Fig. 5(c) very well.

and $J_{kl} \gg \Delta E_{Z,kl}$, which, for the top-right quadrants in Figs. 5(a), 5(e), and 5(i) is not always given. These notions are summarized in Fig. 21. In Fig. 21(a) we plot the energy of the four-spin system 2-1-5-6 as a function of $b_{56}^\dagger - b_{12}^\dagger$ as scanned in Fig. 5(b) with a small exchange between spins 1 and 5 in the chain induced by $b_{15}^\dagger$. The overlap with the four important states in the legend is color-coded and thickness-coded. We observe two avoided crossings, one for $|ST^-\rangle \leftrightarrow |T^-S\rangle$ and the other for $|ST^0\rangle \leftrightarrow |T^0S\rangle$. The fact that the avoided crossings occur at different gate voltages reflects the slightly different requirements for J_{12} and J_{56}. However, the size of both avoided crossings is equal and determined solely by J_{15}.

Finally, we point out that since the readout in PSB is not capable of distinguishing $|T^0\rangle$ from $|T^-\rangle$, we will find more "leakage" features that, while not directly coupling the different subspaces, will lead to deviations from the expected resonant condition positions. This can be

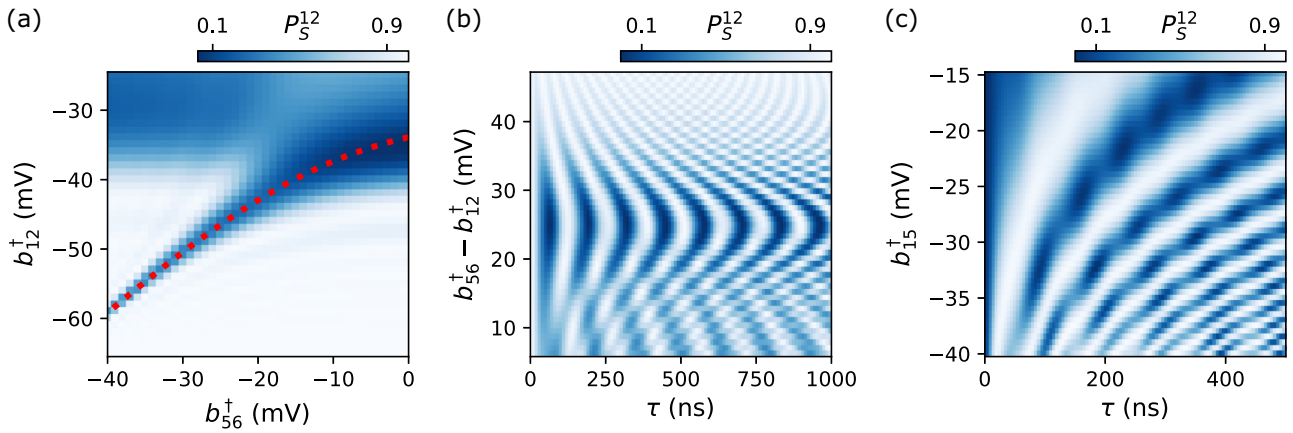

FIG. 24. Simulations of the chain spanned by quantum dots 2, 1, 5, and 6. (a) Simulated singlet return probability P_S^{12} as a function of $b_{56}^\dagger$ and $b_{12}^\dagger$ with an exchange opened between spins 1 and 5. The dotted red line is the same as in Fig. 5(e) and marks the condition $|J_{12} - E_{Z12}| = |J_{56} - E_{Z56}|$. We find good agreement with the data. (b) Resonant $S_{12}T_{56}^-$ condition. We sweep $b_{56}^\dagger$ and $b_{12}^\dagger$ like in the experiment reported in Fig. 5(f) and again report P_S^{12}, finding again good agreement with the data. For low values of $b_{56}^\dagger - b_{12}^\dagger$ we also observe leakage features due to ST^0 oscillations in Q_{12}, just like in the experiment. (c) Resonant $S_{12}T_{56}^0$ oscillations as a function of $b_{15}^\dagger$ at the resonant ST^0 condition. The simulation matches the experimental results in Fig. 5(g) very well.

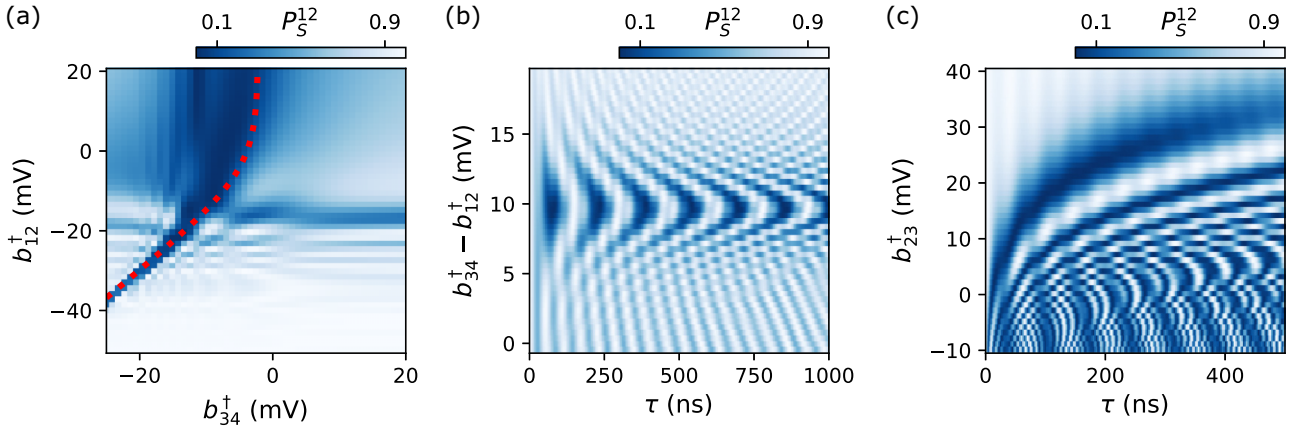

FIG. 25. Simulations of the chain spanned by quantum dots 1, 2, 3, and 4. (a) Simulated singlet return probability P_S^{12} as a function of $b_{34}^\dagger$ and $b_{12}^\dagger$ with an exchange opened between spins 2 and 3. The dotted red line is the same as in Fig. 5(i) and marks the condition $|J_{34} - E_{Z34}| = |J_{12} - E_{Z12}|$. We find good agreement with the data. (b) Resonant $S_{12}T_{34}^-$ condition. We sweep $b_{34}^\dagger$ and $b_{12}^\dagger$ like in the experiment reported in Fig. 5(j) and report P_S^{12}, finding again good agreement with the data except for the leakage features, which are not present in the data, probably due to low visibility. (c) Resonant $S_{12}T_-^{34}$ oscillations as a function of $b_{23}^\dagger$ at the resonant ST^- condition. The simulation matches the experimental results in Fig. 5(k) well.

appreciated in Fig. 21(c), where we record the $S_{12}T_{56}^0$ resonant condition. Apart from the expected diagonal feature, we also observe two horizontal features indicated by the arrows. One is attributed to ST^0 oscillations in Q_{12}, and the other is attributed to ST^- oscillations at the spin-orbit anticrossing of Q_{12}. Apart from the spin-orbit-induced leakage terms, the Hamiltonian that we use to simulate the system contains all the necessary information to reproduce the experimental results.

APPENDIX I: ADDITIONAL DATA FOR THE RESONANT 1256 CONDITION

Figure 22 shows additional measurements of the resonant $S_{12}T_{56}^0$ condition as we change $b_{15}^\dagger$ in steps. We notice the maximum of the oscillation amplitude is always at the same point for $b_{56}^\dagger - b_{12}^\dagger$, which suggests that we have likely compensated the crosstalk to $b_{15}^\dagger$ correctly. The chevron pattern becomes more spread as a result of an increase in J_{15}, which is reflected also by the minimum oscillation frequency in each plot.

1. APPENDIX J: SIMULATIONS OF THE HEISENBERG CHAIN

We perform the simulations of our experiments with the PYTHON package QuTiP and assume that the system evolves under the Heisenberg Hamiltonian defined in Eq. (2). We incorporate the experimentally determined g factors and exchange profiles. For the four-spin chains we operate far from the spin-orbit avoided crossing and therefore omit them in the simulations for simplicity. Our model still captures the relevant parts of the system dynamics. Furthermore, in our analysis we have ignored g-factor modulations due to barrier gate voltages. For high enough exchange, a small deviation of the g factors will not alter the dynamics of the system considerably. Figure 23 simulates the results for Figs. 5(a)–5(c), Fig. 24 pertains to the experimental results reported in Figs. 5(e)–5(g), while Fig. 25 simulates the results for the linear chain shown in Figs. 5(i)–5(k). In Figs. 23–25 the dotted red lines are the same as in the corresponding figures in the main text.

[1] P. Stano and D. Loss, Review of performance metrics of spin qubits in gated semiconducting nanostructures, Nat. Rev. Phys. **4**, 672 (2022).
[2] G. Burkard, T. D. Ladd, A. Pan, J. M. Nichol, and J. R. Petta, Semiconductor spin qubits, Rev. Mod. Phys. **95**, 025003 (2023).
[3] P. Barthelemy and L. M. K. Vandersypen, Quantum dot systems: A versatile platform for quantum simulations, Ann. Phys. **525**, 808 (2013).
[4] C. Volk, A. M. J. Zwerver, U. Mukhopadhyay, P. T. Eendebak, C. J. van Diepen, J. P. Dehollain, T. Hensgens, T. Fujita, C. Reichl, W. Wegscheider, and L. M. K. Vandersypen, Loading a quantum-dot based "Qubyte" register, npj Quantum Inf. **5**, 29 (2019).
[5] C. J. van Diepen, P. T. Eendebak, B. T. Buijtendorp, U. Mukhopadhyay, T. Fujita, C. Reichl, W. Wegscheider, and L. M. K. Vandersypen, Automated tuning of inter-dot tunnel coupling in double quantum dots, Appl. Phys. Lett. **113**, 033101 (2018).
[6] H. Qiao, Y. P. Kandel, K. Deng, S. Fallahi, G. C. Gardner, M. J. Manfra, E. Barnes, and J. M. Nichol, Coherent

multispin exchange coupling in a quantum-dot spin chain, Phys. Rev. X **10**, 031006 (2020).

[7] A. R. Mills, M. M. Feldman, C. Monical, P. J. Lewis, K. W. Larson, A. M. Mounce, and J. R. Petta, Computer-automated tuning procedures for semiconductor quantum dot arrays, Appl. Phys. Lett. **115**, 113501 (2019).

[8] A. S. Rao, D. Buterakos, B. van Straaten, V. John, C. X. Yu, S. D. Oosterhout, L. Stehouwer, G. Scappucci, M. Veldhorst, F. Borsoi, and J. P. Zwolak, Modular autonomous virtualization system for two-dimensional semiconductor quantum dot arrays, Phys. Rev. X **15**, 021034 (2025).

[9] F. Fedele, A. Chatterjee, S. Fallahi, G. C. Gardner, M. J. Manfra, and F. Kuemmeth, Simultaneous operations in a two-dimensional array of singlet-triplet qubits, PRX Quantum **2**, 040306 (2021).

[10] M. T. Mądzik *et al.*, Operating two exchange-only qubits in parallel, arXiv:2504.01191 [quant-ph].

[11] K. Takeda, A. Noiri, T. Nakajima, J. Yoneda, T. Kobayashi, and S. Tarucha, Quantum tomography of an entangled three-qubit state in silicon, Nat. Nanotechnol. **16**, 965 (2021).

[12] S. G. J. Philips, M. T. Mądzik, S. V. Amitonov, S. L. de Snoo, M. Russ, N. Kalhor, C. Volk, W. I. L. Lawrie, D. Brousse, L. Tryputen, B. P. Wuetz, A. Sammak, M. Veldhorst, G. Scappucci, and L. M. K. Vandersypen, Universal control of a six-qubit quantum processor in silicon, Nature **609**, 919 (2022).

[13] L. M. K. Vandersypen, H. Bluhm, J. S. Clarke, A. S. Dzurak, R. Ishihara, A. Morello, D. J. Reilly, L. R. Schreiber, and M. Veldhorst, Interfacing spin qubits in quantum dots and donors—Hot, dense, and coherent, npj Quantum Inf. **3**, 34 (2017).

[14] J. M. Boter, J. P. Dehollain, J. P. van Dijk, Y. Xu, T. Hensgens, R. Versluis, H. W. Naus, J. S. Clarke, M. Veldhorst, F. Sebastiano, and L. M. Vandersypen, Spiderweb array: A sparse spin-qubit array, Phys. Rev. Appl. **18**, 024053 (2022).

[15] C.-A. Wang, V. John, H. Tidjani, C. X. Yu, A. S. Ivlev, C. Déprez, F. van Riggelen-Doelman, B. D. Woods, N. W. Hendrickx, W. I. L. Lawrie, L. E. A. Stehouwer, S. D. Oosterhout, A. Sammak, M. Friesen, G. Scappucci, S. L. de Snoo, M. Rimbach-Russ, F. Borsoi, and M. Veldhorst, Operating semiconductor quantum processors with hopping spins, Science **385**, 447 (2024).

[16] N. W. Hendrickx, W. I. L. Lawrie, M. Russ, F. van Riggelen, S. L. de Snoo, R. N. Schouten, A. Sammak, G. Scappucci, and M. Veldhorst, A four-qubit germanium quantum processor, Nature **591**, 580 (2021).

[17] M. T. Mądzik, S. Asaad, A. Youssry, B. Joecker, K. M. Rudinger, E. Nielsen, K. C. Young, T. J. Proctor, A. D. Baczewski, A. Laucht, V. Schmitt, F. E. Hudson, K. M. Itoh, A. M. Jakob, B. C. Johnson, D. N. Jamieson, A. S. Dzurak, C. Ferrie, R. Blume-Kohout, and A. Morello, Precision tomography of a three-qubit donor quantum processor in silicon, Nature **601**, 348 (2022).

[18] C. A. Stafford and S. Das Sarma, Collective Coulomb blockade in an array of quantum dots: A Mott-Hubbard approach, Phys. Rev. Lett. **72**, 3590 (1994).

[19] T. Hensgens, T. Fujita, L. Janssen, X. Li, C. J. Van Diepen, C. Reichl, W. Wegscheider, S. Das Sarma, and L. M. K. Vandersypen, Quantum simulation of a Fermi–Hubbard model using a semiconductor quantum dot array, Nature **548**, 70 (2017).

[20] E. Barnes, J. M. Nichol, and S. E. Economou, Stabilization and manipulation of multispin states in quantum-dot time crystals with Heisenberg interactions, Phys. Rev. B **99**, 035311 (2019).

[21] J. P. Dehollain, U. Mukhopadhyay, V. P. Michal, Y. Wang, B. Wunsch, C. Reichl, W. Wegscheider, M. S. Rudner, E. Demler, and L. M. K. Vandersypen, Nagaoka ferromagnetism observed in a quantum dot plaquette, Nature **579**, 528 (2020).

[22] R. E. Throckmorton and S. Das Sarma, Studying many-body localization in exchange-coupled electron spin qubits using spin-spin correlations, Phys. Rev. B **103**, 165431 (2021).

[23] X. Wang, E. Khatami, F. Fei, J. Wyrick, P. Namboodiri, R. Kashid, A. F. Rigosi, G. Bryant, and R. Silver, Experimental realization of an extended Fermi-Hubbard model using a 2D lattice of dopant-based quantum dots, Nat. Commun. **13**, 6824 (2022).

[24] J. Knörzer, C. J. van Diepen, T.-K. Hsiao, G. Giedke, U. Mukhopadhyay, C. Reichl, W. Wegscheider, J. I. Cirac, and L. M. K. Vandersypen, Long-range electron-electron interactions in quantum dot systems and applications in quantum chemistry, Phys. Rev. Res. **4**, 033043 (2022).

[25] D. Buterakos and S. Das Sarma, Magnetic phases of bilayer quantum-dot Hubbard model plaquettes, Phys. Rev. B **108**, 235301 (2023).

[26] C.-A. Wang, C. Déprez, H. Tidjani, W. I. L. Lawrie, N. W. Hendrickx, A. Sammak, G. Scappucci, and M. Veldhorst, Probing resonating valence bonds on a programmable germanium quantum simulator, npj Quantum Inf. **9**, 58 (2023).

[27] A. Nico-Katz, G. Jaliel, P. Atkinson, T. A. Mitchell, D. A. Ritchie, C. G. Smith, and S. Bose, Identifying many-body localization in realistic dot arrays, arXiv:2301.08246 [cond-mat.dis-nn].

[28] C. van Diepen, T.-K. Hsiao, U. Mukhopadhyay, C. Reichl, W. Wegscheider, and L. Vandersypen, Quantum simulation of antiferromagnetic Heisenberg chain with gate-defined quantum dots, Phys. Rev. X **11**, 041025 (2021).

[29] M. Lodari, N. W. Hendrickx, W. I. L. Lawrie, T.-K. Hsiao, L. M. K. Vandersypen, A. Sammak, M. Veldhorst, and G. Scappucci, Low percolation density and charge noise with holes in germanium, Mater. Quantum Technol. **1**, 011002 (2021).

[30] F. Vigneau, F. Fedele, A. Chatterjee, D. Reilly, F. Kuemmeth, M. F. Gonzalez-Zalba, E. Laird, and N. Ares, Probing quantum devices with radio-frequency reflectometry, Appl. Phys. Rev. **10**, 021305 (2023).

[31] T.-K. Hsiao, P. Cova Fariña, S. Oosterhout, D. Jirovec, X. Zhang, C. van Diepen, W. Lawrie, C.-A. Wang, A. Sammak, G. Scappucci, M. Veldhorst, E. Demler, and L. Vandersypen, Exciton transport in a germanium quantum dot ladder, Phys. Rev. X **14**, 011048 (2024).

[32] X. Zhang, E. Morozova, M. Rimbach-Russ, D. Jirovec, T.-K. Hsiao, P. C. Fariña, C.-A. Wang, S. D. Oosterhout, A. Sammak, G. Scappucci, M. Veldhorst, and L. M. K. Vandersypen, Universal control of four singlet–triplet qubits, Nat. Nanotechnol. **20**, 209 (2024).

[33] J. Levy, Universal quantum computation with spin-1/2 pairs and Heisenberg exchange, Phys. Rev. Lett. **89**, 147902 (2002).

[34] J. R. Petta, A. C. Johnson, J. M. Taylor, E. A. Laird, A. Yacoby, M. D. Lukin, C. M. Marcus, M. P. Hanson, and A. C. Gossard, Coherent manipulation of coupled electron spins in semiconductor quantum dots, Science **309**, 2180 (2005).

[35] D. Jirovec, A. Hofmann, A. Ballabio, P. M. Mutter, G. Tavani, M. Botifoll, A. Crippa, J. Kukucka, O. Sagi, F. Martins, J. Saez-Mollejo, I. Prieto, M. Borovkov, J. Arbiol, D. Chrastina, G. Isella, and G. Katsaros, A singlet-triplet hole spin qubit in planar Ge, Nat. Mater. **20**, 1106 (2021).

[36] D. Loss and D. P. DiVincenzo, Quantum computation with quantum dots, Phys. Rev. A **57**, 120 (1998).

[37] Z. Zhou, Y. Li, Z. Wu, X. Ma, S. Fan, and S. Huang, The exchange interaction between neighboring quantum dots: Physics and applications in quantum information processing, J. Semiconduct. **45**, 101701 (2024).

[38] F. Martins, F. K. Malinowski, P. D. Nissen, E. Barnes, S. Fallahi, G. C. Gardner, M. J. Manfra, C. M. Marcus, and F. Kuemmeth, Noise suppression using symmetric exchange gates in spin qubits, Phys. Rev. Lett. **116**, 116801 (2016).

[39] D. Jirovec, P. M. Mutter, A. Hofmann, A. Crippa, M. Rychetsky, D. L. Craig, J. Kukucka, F. Martins, A. Ballabio, N. Ares, D. Chrastina, G. Isella, G. Burkard, and G. Katsaros, Dynamics of hole singlet-triplet qubits with large g-factor differences, Phys. Rev. Lett. **128**, 126803 (2022).

[40] J. Saez-Mollejo, D. Jirovec, Y. Schell, J. Kukucka, S. Calcaterra, D. Chrastina, G. Isella, M. Rimbach-Russ, S. Bosco, and G. Katsaros, Exchange anisotropies in microwave-driven singlet-triplet qubits, Nat. Commun. **16**, 3862 (2025).

[41] P. M. Mutter and G. Burkard, All-electrical control of hole singlet-triplet spin qubits at low-leakage points, Phys. Rev. B **104**, 195421 (2021).

[42] D. J. Niegemann, V. El-Homsy, B. Jadot, M. Nurizzo, B. Cardoso-Paz, E. Chanrion, M. Dartiailh, B. Klemt, V. Thiney, C. Bäuerle, P.-A. Mortemousque, B. Bertrand, H. Niebojewski, M. Vinet, F. Balestro, T. Meunier, and M. Urdampilleta, Parity and singlet-triplet high fidelity readout in a silicon double quantum dot at 0.5 K, PRX Quantum **3**, 040335 (2022).

[43] L. Mauro, E. A. Rodríguez-Mena, M. Bassi, V. Schmitt, and Y.-M. Niquet, Geometry of the dephasing sweet spots of spin-orbit qubits, Phys. Rev. B **109**, 155406 (2024).

[44] P. C. Fariña, D. Jirovec, X. Zhang, E. Morozova, S. D. Oosterhout, S. Reale, T.-K. Hsiao, G. Scappucci, M. Veldhorst, and L. M. K. Vandersypen, Site-resolved magnon and triplon dynamics on a programmable quantum dot spin ladder, arXiv:2506.08663.

[45] W. Ha, S. D. Ha, M. D. Choi, Y. Tang, A. E. Schmitz, M. P. Levendorf, K. Lee, J. M. Chappell, T. S. Adams, D. R. Hulbert, E. Acuna, R. S. Noah, J. W. Matten, M. P. Jura, J. A. Wright, M. T. Rakher, and M. G. Borselli, A flexible design platform for Si/SiGe exchange-only qubits with low disorder, Nano Lett. **22**, 1443 (2021).

[46] A. J. Weinstein *et al.*, Universal logic with encoded spin qubits in silicon, Nature **615**, 817 (2023).

[47] H. C. George *et al.*, 12-spin-qubit arrays fabricated on a 300 mm semiconductor manufacturing line, Nano Lett. **25**, 793 (2024).

[48] D. Jirovec, P. C. Fariña, S. Reale, S. D. Oosterhout, X. Zhang, S. deSnoo, A. Sammak, G. Scappucci, M. Veldhorst, and L. M. K. Vandersypen, Data underlying the publication: "Mitigation of exchange crosstalk in dense quantum dot arrays" (2025).

[49] S. Geyer, B. Hetényi, S. Bosco, L. C. Camenzind, R. S. Eggli, A. Fuhrer, D. Loss, R. J. Warburton, D. M. Zumbühl, and A. V. Kuhlmann, Anisotropic exchange interaction of two hole-spin qubits, Nat. Phys. **20**, 1152 (2024).